Syntaxin-2 inhibits phagocytic uptake but promotes phagolysosome formation in macrophages

Suman Samanta[1], Abhrajyoti Nandi[1], Rupak Datta[1]*, Subhankar Dolai[2]*

[1]Department of Biological Sciences, Indian Institute of Science Education and Research Kolkata, Mohanpur, West Bengal, India.

[2]Department of Biotechnology, The University of Burdwan, West Bengal, India.

***Address correspondence to:**

Subhankar Dolai, Ph.D., Room 6, Department of Biotechnology, The University of Burdwan, Golapbag Campus, Burdwan - 713104, West Bengal, India. Email: subhankar.dolai@gmail.com

Rupak Datta, Ph.D.; Room 221, Department of Biological Sciences, Indian Institute of Science Education and Research Kolkata, Mohanpur, Nadia - 741246, West Bengal, India. E-mail: rupakdatta@iiserkol.ac.in

Running title: Opposing role of syntaxin-2 in phagosome biogenesis and maturation.

Key words: SNARE, phagocytosis, lysosome, Fcγ receptors, TFEB

Abstract

Phagocytosis engulfs unwanted particles into phagosomes for lysosome-mediated degradation in phagolysosomes. Both uncontrolled and defective phagocytosis posits detrimental physiologic consequences. We show here, syntaxin-2 (Stx2), a poorly characterized SNARE in phagocytes, critically controls macrophage phagosome, lysosome, and phagolysosome biogenesis for balancing uptake and clearance. Stx2 is predominantly expressed on inner and outer surfaces of plasmalemma, early endosomes, VAMP4-positive compartments, and phagosomes. Depletion of Stx2 (Stx2-KD) increases the entrapment and uptake of IgG-opsonized particles by enhancing formation and expansion of phagocytic cups, driven by increased trafficking of early endosomes and VAMP4-positive post-Golgi compartments. Additionally, Stx2-KD augments the surface expression of Fcγ receptors, nuclear translocation of TFEB, and biogenesis of functional lysosomes. Interestingly, Stx2-KD impedes phagosome acquisition of late endosomes, lysosomes, and vacuolar ATPase; depleting phagosomal cathepsin contents and acidification. Consequently, Stx2-KD enables macrophages to efficiently uptake IgG-opsonized *Escherichia coli* but impairs their digestion. Collectively, Stx2 regulates macrophage phagocytosis by controlling excess uptake of phagocytic particles but by facilitating their lysosomal clearance.

Introduction

Phagocytosis, a conserved cellular process, entails engulfment and subsequent disposal of large (>0.5 µm in diameter) extracellular particles (Aderem and Underhill, 1999; Flannagan et al., 2012). The process begins with the interaction of phagocytic particles with specific cell surface receptors, such as Fcγ receptors (FcRs) of immunoglobulin G (IgG) (Freeman and Grinstein, 2014). Activation of phagocytic receptors triggers actin-dependent restructuring of the plasmalemma into cup-like formations (phagocytic cups) around the particles (Freeman and Grinstein, 2014; Swanson, 2008). The expansion of phagocytic cups leads to the closure and sequestration of particles within phagosomes (Freeman and Grinstein, 2014; Niedergang and Grinstein, 2018). These nascent phagosomes mature into acidic, hydrolytic enzyme-rich phagolysosomes, where degradation occurs (Botelho and Grinstein, 2011; Roy et al., 2004; Vieira et al., 2002). Professional phagocytes such as macrophages, dendritic cells and granulocytes deploy phagocytosis to eliminate pathogens, cellular debris, and non-living particles from organisms (Flannagan et al., 2012; Stuart and Ezekowitz, 2005). Phagocytes also bridge innate and adaptive immunity by presenting fragments of engulfed particles as antigens to T cells (Mantegazza et al., 2013). However, uncontrolled phagocytosis leads to hemophagocytosis, tissue damage, organ failure and neurodegeneration (Al-Samkari and Berliner, 2018; Butler et al., 2021); while impaired clearance of phagocytic bodies develops autoimmune and neurodegenerative diseases (Kleinberger et al., 2014; Munoz et al., 2010). Controlled uptake and efficient clearance of phagocytic particles for optimal phagocytosis are therefore critical for disease defense and organismal homeostasis (Arandjelovic and Ravichandran, 2015).

Expansion of phagocytic cups and biogenesis of phagosomes are prerequisites for any form of phagocytosis that require regulated membrane trafficking from intracellular compartments (Flannagan et al., 2012). The maturation of phagosomes into phagolysosome also requires sequential fusions with endolysosomal compartments (Becken et al., 2010; Vieira et al., 2002). In eukaryotic cells, SNARE proteins act on the terminal step of intracellular compartmental trafficking by mediating membrane fusions (Jahn and Scheller, 2006; Sudhof and Rothman, 2009). Typically, target membrane-localized t-/Q-SNAREs (syntaxins and SNAPs) combine with vesicle-associated v-/R-SNAREs (like VAMPs) to form a four-helix trans-SNARE complex that mediates membrane merger (Jahn and Scheller, 2006; Sudhof and Rothman, 2009). Previous works validated SNARE-dependent delivery of early endosomes/VAMP2 (Hackam et al., 1998), recycling endosomes/VAMP3 (Bajno et al., 2000; Niedergang et al., 2003), late endosomes/VAMP7 (Braun et al., 2004) and lysosomes/synaptotagmin VII (Czibener et al., 2006;

Rao et al., 2004) to be crucial for phagocytosis. Thus the identity of intracellular compartments, their contributions to phagocytosis and the participating v-/R-SNAREs are well acknowledged. However, mechanisms that regulate differential membrane acquisition from non-lytic and lytic compartments that control phagocytic uptake and maturation of phagosome to determine the retention or clearance of internalized substances within phagolysosomes remain enigmatic.

Contrary to pro-fusion roles, some SNAREs interfere with other cis-SNAREs to inhibit or fine-tune (inhibitory/i-SNAREs) membrane fusions (Paumet et al., 2009; Varlamov et al., 2004). Syntaxin-2 (Stx2) was initially discovered as an extracellular epithelial morphogen called epimorphin (Hirai et al., 1992) and later its intracellular version was characterized as a t-/Q-SNARE (Bennett et al., 1993). Stx2 is unique amongst the t-/-Q SNARE in showing fusion-neutral (in platelets) (Ye et al., 2012), fusion-competent (kidney and goblet cell) (Low et al., 2003; Wojnacki et al., 2023), and i-SNARE properties (in pancreatic acinar and beta cells) (Dolai et al., 2018; Kang et al., 2022; Zhu et al., 2017). These variegated features of Stx2, coupled with its prominent expression in macrophages (Hackam et al., 1996; Murray et al., 2005; Pagan et al., 2003) but unknown functions in phagocytosis, led us to hypothesize that Stx2 might be critical in controlling various incoming trafficking to shape the course of phagocytosis. Our findings show that Stx2 indeed demonstrates pleiotropic and contrasting roles in macrophage phagocytosis. Stx2 inhibits trafficking of non-lytic early endosomes and VAMP4-positive post Golgi compartments for phagocytic cup expansion and phagosome biogenesis. However, Stx2 is found essential for phagosome acquisition of lytic late endosomes and lysosomes, and thereby maturation of phagosomes into phagolysosomes. Additionally, we found that Stx2 limits the macrophage expression of FcRs, which is known to facilitate plasmalemmal remodelling for phagocytic cup formation and thereby phagocytosis. Moreover, we observed that Stx2 is also critical for controlling lysosome biogenesis in macrophages by regulating the nuclear translocation of transcription factor EB (TFEB) that governs lysosome gene expressions and functions.

Results

Stx2 is localized on inner and outer plasmalemma, VAMP4-positive and early endosome compartments, and phagosomes of RAW 264.7 macrophage cells

To unveil Stx2 functions in macrophage phagocytosis, we first conducted a detailed investigation on subcellular distribution of endogenous Stx2 in RAW 264.7 macrophage cells. Using confocal immunofluorescence imaging on RAW 264.7 cells, we detected a predominant but discontinuous presence of Stx2 on plasmalemma that lined up with β-actin/ACTB (Fig 1 A). We also observed

some punctate intracellular appearance of Stx2 (Fig 1 A). This pattern of distribution of Stx2 is consistent with other plasmalemmal Stxs of J774 (Hackam et al., 1996). In few other cells, Stx2 is also expressed on the extracellular surface of the plasmalemma (Flaumenhaft et al., 2007; Fritsch et al., 2002; Hirai et al., 2001; Kang et al., 2022). Close inspection of plasmalemmal distribution of Stx2 in RAW 264.7 cells indicates the possibility of extracellular presence of Stx2 to some extent (Fig 1 A, arrows). To verify this, we performed confocal immunofluorescence imaging for Stx2 and ACTB on intact, non-permeabilized RAW 264.7 cells (Fig. 1 A and B). This produced only punctate signal for Stx2 at the cell periphery but not for ACTB that resides beneath the plasmalemma (Fig 1 B). To testify the specificity of the Stx2 signal, we pre-incubated anti-Stx2 antibody with purified rat Stx2 that nearly eliminated the surface signal for Stx2 (Fig 1 C). Further, flow cytometry (FACS) analyses of intact cells that surface-labeled for Stx2 showed ~14 fold (Control: 78, Stx2-KD: 1,118) shift in mean fluorescence intensity (MFI) relative to Control cells labeled with only flurophore-conjugated secondary antibody (Fig 1 D and E). These results suggest that fractions of the plasmalemmal Stx2 are also expressed on the outer surface of RAW 264.7 cells. We then attempted to ascertain the intracellular residence of Stx2 by confocal immunofluorescence imaging of Stx2, along with bonafide markers of various cell organelles. We observed some degree of Stx2 co-localization with early endosomes (RAB5A, Fig 1 F) and VAMP4-positive compartments (Fig 1 G). VAMP4 is found in trans-Golgi network and in the sorting and recycling endosomes (Shui et al., 2008; Tran et al., 2007). Stx2 is thus expected to share these intracellular locations. However, we could not detect Stx2 localization with VAMP7 (late endosomes) and LAMP1 (lysosomes) (Fig S1 A and B). In accordance to an earlier report on J774 cells (Hackam et al., 1996), we also obtained abundant presence of Stx2 around the periphery of opsonized zymosan particle (OPZ)-containing phagosomes (Fig 1 H). Immunoblot probing of purified phagosomes further validated Stx2 presence in phagosomes (Fig 1 I). Collectively, these data demonstrate that Stx2 is distributed on inner/outer leaflet of plasmalemma, along with early endosomes, VAMP4-positive compartments and phagosomes of macrophages.

Stx2-KD improves macrophage efficacy for phagocytic uptake of IgG-opsonized particles

To evaluate Stx2 functions in macrophages, pertaining to phagocytosis, we established a Stx2 depleted (Stx2-KD: ~70%) RAW 264.7 cell line by stably expressing shRNAs targeted to mouse Stx2 (Fig. 2 A and B; S2 A and B). A parallel Control cell line was generated by expressing nonspecific scrambled-shRNA (sc-shRNA) that did not affect endogenous expression of Stx2

(Fig. 2 A and B; S2 A and B). Confocal immunofluorescence imaging of Stx2 further confirmed reduction of Stx2 level in Stx2-KD cells (Fig. 2C). In order to gain an indication of Stx2-KD impact on phagocytosis, we incubated Control and Stx2-KD macrophages with IgG-opsonized fluorescent polystyrene beads (OPFB, 2 µm diameter: OPFB-2) for 15 min to 60 min (Fig. S2, C-E). Differential interference contrast (DIC) and confocal fluorescence imaging showed increased number of OPFB-2 inside the periphery of Stx2-KD macrophages at all the investigated time points (Fig. S2 C). Quantification revealed significantly increased numbers of OPFB-2 were associated with Stx2-KD macrophages over the incubation period (Fig. S2 D). Further, FACS analysis of 30 min and 60 min OPFB-2 incubated cells showed ~ 2.2 fold (Control: 1865; Stx2-KD: 4149) and ~ 2.7 fold (Control: 3200; Stx2-KD: 8728) increments in MFI (i.e. the increased number of OPFB-2 association/cell) in Stx2-KD cells, respectively (Fig. S2 E). Stx2-KD thus seemed to augment macrophage engulfment (partial and full) capacity for OPFB-2.

To get better perspective on phagocytic ability of Stx2-KD cells, we exposed macrophages to larger-sized (4-5 µm diameter) opsonized zymosan red-fluorescent particles (OPZR) (Czibener et al., 2006). Here, we also immunolabeled macrophages for Stx2 to visualize its expression and to directly correlate the change in phagocytic activity with endogenous Stx2 level (Fig. 2 D). Despite ~ 10X larger volume than OPFB-2, the confocal fluorescence microscopy assessment revealed a surge in OPZR uptake in Stx2-KD macrophages (15 min: ~ 1.8 fold; 30 min: ~ 1.5 fold and 60 min: 1.6 fold) (Fig. 2E), which are comparable to OPFB-2 phagocytosis (Fig. S2, C-E). We thus next challenged the cells with even larger opsonized red-fluorescent beads (OPFB, 10 µm diameter: OPFB-10; ~ 10 X larger volume to OPZR) for 30 min and 60 min (Fig. 2 F). We also probed the cells for ACTB to demarcate the membrane periphery and the phagocytosis spots (Fig. 2 F). Macrophages were able to engulf maximum of one OPFB-10/nucleus as observed by confocal imaging (Fig. 2 F). However, the percentage of cells that engulfed OPFB-10 was significantly higher amongst the Stx2-KD cells at both 30 min (Control: ~ 11.6%; Stx2-KD: ~ 27%) and 60 min (Control: ~ 20%; Stx2-KD: 41.6%) (Fig. 2 G). Finally, to evaluate the phagocytosis in larger population of cells, we analyzed OPZR and OPFB-10 incubated cells by FACS (Fig. 2 H and I). Stx2-KD cells showed modest increment for OPZR positivity in 30 min (Control: 39.7% vs Stx2-KD: 48.2%) and 60 min (Control: 49% vs Stx2-KD: 62%), suggesting increased phagocytic activity. The MFI, hence the engulfed OPZR particles/cell in Stx2-KD cells was 1.5 fold higher at 30 min (Control MFI: 8,489; Stx2-KD MFI: 12,643) and 1.6 fold higher at 60 min (Control MFI: 10,801; Stx2-KD MFI: 17450) (Fig. 2H). Since, macrophages were able to engulf only one OPFB-10/cell during 60 min of incubation (Fig. 2 F), we observed a narrow peak at the same spot on X-

axis for both Control and Stx2-KD cells. The MFI was also comparable in both cells (Control MFI: 8,156; Stx2-KD MFI: 8,210). However, the percentage of cells engulfed OPFB-10 was ~ 1.7 fold higher (Control: 4.4%; Stx2-KD: 8.2%) in Stx2-KD cells (Fig. 2 I). Collectively, our results testify increased phagocytosis efficacy of Stx2-KD cells for IgG-opsonized particles.

Stx2-KD increases formation and expansion of phagocytic cups for efficient particle trapping and phagocytosis

Engagements of IgG-opsonized particles with macrophages develop phagocytic cups that facilitate the grasping of phagocytic particles (Flannagan et al., 2012; Swanson, 2008). Subsequent extension of the phagocytic cups leads to closure and engulfment of particles within phagosomes (Flannagan et al., 2012; Swanson, 2008). Given that Stx2-KD enhances the uptake of IgG-opsonized particles (Fig. 2), we utilized scanning electron microscopy (SEM) to scrutinize alterations in external plasmalemmal morphology during phagocytosis. At an earlier time point (5 min) of incubation, IgG-opsonized polystyrene beads (OPB, 3 µm diameter: OPB-3) exhibited ~ 2.2 fold increment in attachment (Control: 1.188 OPB-3/cell; Stx2-KD: 2.66 OPB-3/cell) to the surface of Stx2-KD RAW 264.7 cells (Fig. 3 A and C). Additionally, the emergence of phagocytic cups was evident in Stx2-KD cells (Fig. 3 A and B). The numbers of attached OPB-3 were further increased by ~ 2.5 fold in Stx2-KD cells after 10 min (Control: 1.27 OPB-3/cell; Stx2-KD: 3.19 OPB-3/cell), accompanied by prominent appearance of phagocytic cups (Fig. 3 A -C). By 30 min, there was a marked decrease in attached OPB-3 numbers in both Stx2-KD and Control cells, with the majority of the attached OPB-3 internalized (Fig. 3 A-C). For a quantitative assessment of plasmalemmal extension, we measured the area of phagocytic cups by calculating the OPB-3-covered membrane area (in μm^2), expressed as mean (Fig. 3 D) or cumulative values (Fig. 3 E). Analysis of mean area demonstrated ~ 1.4 fold increment over 5 min (Control: 0.789 μm^2/OPB-3; Stx2-KD: 1.113 μm^2/OPB-3) and ~ 1.6 fold increment over 10 min (Control: 1.17 μm^2/OPB-3; Stx2-KD: 1.897 μm^2/OPB-3) (Fig. 3D). Analysis of plasmalemma wrapped cumulative bead area/cell showed ~ 2.3 fold increment over 5 min (Control: 0.95 μm^2/cell; Stx2-KD: 2.16 μm^2/cell), ~ 3.7 fold increment over 10 min (Control: 1.17 µm2/cell; Stx2-KD: 4.3 µm2/cell) and ~3.6 fold increase at 30 min (Control: 2.53 µm2/cell; Stx2-KD: 9.2 µm2/cell) in Stx2-KD cells (Fig. 3E). Since, most of the surface adherent OPB-3 was taken up by 30 min; we challenged both Control and Stx2-KD macrophages with larger OPFB-10 for 30 min, followed by immunostaining for ACTB (Fig. 3 F). Stacked confocal images showed that Stx2-KD macrophages were able to expand phagocytic cups more efficiently to cover larger portions of the OPFB-10 (Fig. 3 F).

Quantitative analysis showed mean OPFB-10 surface area (in μm^2) enveloped with membrane was significantly larger by ~ 1.3 fold (Control: 57.59 μm^2/OPFB-10; Stx2-KD: 73.76 μm^2/OPFB-10) in Stx2-KD macrophages (Fig. 3 G). Collectively, these data suggest that Stx2-KD macrophages are more proficient in forming phagocytic cups and their expansion for enhanced particle trapping and phagocytosis.

Stx2-KD elevates FcR expression and trafficking of early endosomes and VAMP4-positive post-Golgi compartments for phagocytosis

Enhanced formation of phagocytic cups with prominent appearance of actin in Stx2-KD macrophages (Fig. 3) suggest extensive membrane remodelling by FcRs (Swanson and Hoppe, 2004). We therefore examined surface expression of FcRs by FACS that showed ~2.5 fold increment in MFI in Stx2-KD cells (Control: 377; Stx2-KD: 927) over Control macrophages (Fig. 4 A and B). Improved expansion of phagocytic cups and phagocytosis in Stx2-KD macrophages (Fig. 3 and Fig. 2) essentially needs to harness membranes from various intracellular reservoirs to facilitate expansion, sealing, and the formation of phagosomes (Flannagan et al., 2012; Shui et al., 2008). We therefore next aimed to identify and compare the contributions of specific intracellular compartments involved (Fig. 4 C-M). We first purified phagosomes from both Control and Stx2-KD cells, exposed briefly (30 min) to OPB (0.8 µm diameter; OPB-0.8) to obtain the nascent phagosome-enriched fraction. Immunoblot detection and quantification revealed ~ 1.7 fold increased concentration of the early endosome protein RAB5A in Stx2-KD macrophage derived phagosomes (Fig. 4 C and D). We also observed ~ 1.43 fold increase in the phagosome content of R-SNARE protein VAMP4 in Stx2-KD macrophages (Fig. 4 C and F). VAMP4 has been shown to traffic through recycling and sorting endosomes to enrich trans-Golgi network, which is known to be absent from FcR-induced phagosomes (Cebrian et al., 2011; Desjardins et al., 1994). To distinguish the delivery of Golgi and VAMP4-positive post Golgi compartments, we probed the phagosome fractions with the bonafide trans-Golgi dwelling protein golgin-160. Consistent to the earlier reports (Cebrian et al., 2011; Desjardins et al., 1994) we could not detect golgin-160 (Fig. 4 C and G), suggesting contributions from post-Golgi VAMP4-positive compartments. Interestingly, incorporation of VAMP3, a recycling endosome v-/R-SNARE (Bajno et al., 2000) was decreased by ~ 2.6 fold in Stx2-KD phagosomes (Fig. 4 C and E). The contributions from late endosomes (VAMP7) (Braun et al., 2004) and lysosomes (VAMP8) (Diao et al., 2015) were also depleted by 1.42 fold and 2.9 fold (Fig. 4 C, H and I) respectively. To verify these observations and to visualize the presence of these compartments at the phagocytic cups,

we imaged both Control and Stx2-KD macrophages that partially engulfed OPFB-10 (Fig. 4, J-M). The VAMP3 antibody did not work for immunofluorescence study. However, imaging with RAB5A and VAMP4 showed increased staining at the phagocytic cup in Stx2-KD cells (Fig. 4 J and K). We also detected strong fluorescence signal from the top of the OPFB-10 during RAB5A imaging. Since that region is beyond the reach of the phagocytic cup, we ignored them as nonspecific and only considered signals coming directly from phagocytic cups or from the edge of the beads. Similar staining with VAMP7 (Fig. 4 L) and VAMP8 (Fig. 4 M) showed their reduced presence in the Stx2-KD phagocytic cups. Altogether, our data show that Stx2-KD endorses expansion of phagocytic cups and biogenesis of phagosomes by elevated trafficking of early endosomes and VAMP4-positive post-Golgi compartments in macrophages.

Stx2-KD boosts biogenesis of functional lysosomes in macrophages

Intrigued by the heightened expression of VAMP8 (Fig. 4 C and I), a lysosomal SNARE protein (Diao et al., 2015), we postulated that Stx2-KD might also augment lysosome biogenesis in macrophages. To investigate, we initially stained Control and Stx2-KD cells with LysoTracker Red DND-99, which labels acidic endolysosomes, and subjected them to FACS analysis (Fig. 5 A). We observed ~ 1.6 fold increase in the MFI (Control: 4913; Stx2-KD: 8004) in Stx2-KD cells (Fig. 5A). Additionally, confocal imaging of LysoTracker Red DND-99 stained macrophages showed notable increase in both the abundance and intensity of red fluorescent puncta within Stx2-KD cells (Fig. 5 B), which were ~ 1.8 higher (Control: 4.4; Stx2-KD: 8.1) in MFI (Fig. 5 C). These findings imply a sprawling presence of lysosomes and their efficient acidification by v-ATPase in Stx2-KD macrophages. We then directly visualized cellular lysosomes by immunostaining lysosome membrane protein LAMP1 and by imaging them using a confocal microscope (Fig. 5 D). Further, we assessed LAMP1 expression by western blot (Fig. 5 F). Quantification of LAMP1 fluorescence intensity (Fig. 5 E) and LAMP1 band density (Fig. 5 G) disclosed a consistent ~ 1.6 fold and ~ 2 fold rise in LAMP1 content in Stx2-KD macrophages. Moreover, the expression of major lysosomal hydrolases like cathepsin L (CTSL), cathepsin B (CTSB), and cathepsin D (CTSD) was also upregulated in Stx2-KD cells (Fig. 5, H-M). Notably, along with their increased expression, the processing of cathepsins was also enhanced, that resulted in increased production of catalytically active mature forms in Stx2-KD macrophages (Fig. 5 J). Further, an elevated basal autophagic flux, as evidenced by heightened LC3-II to LC3-I ratio and concomitant degradation of the autophagy substrate protein P62/PQSTM1 (Fig. 5, N-P) proves enhanced catalytic activity of lysosomes in Stx2-KD macrophages (Fig. 5, N-P). Taken together, these data

suggest that Stx2-KD promotes lysosomal biogenesis, acidification, and degradative capacity in macrophages.

Stx2-KD activates TFEB nuclear translocation in macrophages

The MiTF family of transcription factors (TFEB, TFE3, MITF and TFEC) regulate lysosome biogenesis by controlling expression of a large number of lysosomal genes (Sardiello et al., 2009). Amongst, TFEB has emerged as a key regulator governing lysosomal gene expression and function (Settembre et al., 2011). To determine whether TFEB is also involved in increased biogenesis and improved functionality of lysosomes upon Stx2-KD (Fig 5), we first examined the TFEB status in Control and Stx2-KD macrophages (Fig. 6, A-C). We did not observe any change in expression of TFEB in Stx2-KD macrophages (Fig. 6 A and B). Given that the TFEB functionality relies on its translocation to the nucleus, we next examined cellular distribution of TFEB by immunofluorescence imaging (Fig. 6 C). We observed prominent nuclear presence of TFEB in resting Stx2-KD cells, while in Control cells TFEB was mostly localized at the nuclear periphery and extra nuclear locations (Fig. 6 C). The lysosomal contents in Stx2-KD cells were also remained constantly high as indicated by extensive LAMP1 staining (Fig. 6 C). We further extended our investigation to see if Stx2-KD can maintain high lysosome content during phagocytosis. To examine this we challenged macrophages with OPB-3 for 15 to 60 min and probed them by western blot for LAMP1, CTSL and CTSB (Fig. 6 D). We observed abundant and increased expression for LAMP1 and cathepsins (CTSL and CTSB) in Stx2-KD macrophages (Fig. 6, D-G). FcRs mediated phagocytosis was earlier implicated in increased biogenesis of lysosomes through TFEB activation (Gray et al., 2016). Coupled with increased expression of FcRs in Stx2-KD macrophages (Fig. 4 A), we also observed heightened nuclear translocation of TFEB in Stx2-KD macrophages upon OPB-3 phagocytosis (Fig. 6 H). Taken together, we conclude that Stx2-KD can induce nuclear translocation of TFEB. TFEB translocation further increases during IgG-opsonized particle phagocytosis, which could be aided by enhanced expression of FcRs.

Stx2-KD delays phagosome maturation and acidification in macrophages

Enhanced biogenesis of phagosomes and lysosomes (Fig. 2 and Fig. 5), paired with reduced acquisition of the late endosome and lysosome v-/R-SNARE proteins VAMP7 (Fig. 4 C and H) and VAMP8 (Fig. 4 C and I) during the initial phase of phagosome formation prompted us to investigate how Stx2-KD could impact the maturation of phagosomes into degradative phagolysosome compartments. To delineate the course of phagosome maturation, we exposed

both Control and Stx2-KD macrophages to OPZ for 15 to 60 min (Fig. 7 A). We first assessed phagosome acquisition of the lysosome marker protein LAMP1 using confocal immunofluorescence imaging (Fig. 7 A). In line with our prior observations (Fig. 2), Stx2-KD macrophages engulfed more OPZ particles throughout the experimental timeframe (Fig. 7 A). However, careful observation revealed a gradual and prominent increase in LAMP1 fluorescence intensity around the phagosomes over time in Control cells (Fig. 7 A). In contrast, despite possessing higher numbers of phagosomes and lysosomes, Stx2-KD macrophages exhibited reduced LAMP1 fluorescence signal from phagosomes (Fig. 7 A). Moreover, the MFI of the phagosomes in Stx2-KD cells also remained significantly lower and increased only marginally compared to Control cell phagosomes (Fig. 7 A and B). Concurrently, the presence of CTSL, CTSB and CTSD also remained low in Stx2-KD phagosomes, as indicated by their reduced fluorescence intensity (Fig. 7 C and D). To validate these observations in larger population of phagosomes, and to gauge the presence of catalytically active mature forms of cathepsins within phagosomes, we next purified phagosomes from 1.5 hr (1 hr uptake and 30 min maturation) OPB-0.8 fed Control and Stx2-KD macrophages and probed them for CTSL, CTSB and CTSD (Fig. 7 E). Purified phagosomes from Stx2-KD macrophages show reduced amount of mature forms of CTSL and CTSB (Fig. 7 E). Interestingly, despite the comparable presence of immature form of CTSD in both Control and Stx2-KD phagosomes (Fig. 7 E), the content of mature CTSD was very low in Stx2-KD phagosomes (Fig. 7 E and I). Since the CTSD processing to the mature form relies on CTSL and CTSB activity (Laurent-Matha et al., 2006), our observation further suggests that in addition to their reduced phagosomal presence, the proteolytic activity of CTSL and CTSB were also low in phagosomes from Stx2-KD macrophages. As cathepsins remain active in acidic pH, we additionally probed phagosomes for vacuolar ATPase subunit ATP6V1A, which showed reduced presence in Stx2-KD phagosomes (Fig. 7 E and J), suggesting reduced phagosome acidification. To confirm this we allowed Control and Stx2-KD cells to engulf pHrodo red zymosan BioParticles (pHRZ) that become highly fluorescent in acidic pH (Fig. 7 K). Internalized pHRZ particles in Control cells produced bright red fluorescence upon 30 min that further increased at 60 min (Fig. 7 K and L). However, pHRZ particle fluorescence intensity remained consistently dim within Stx2-KD macrophages (Fig. 7 K and L). The MFI of the pHRZ particles were also remained significantly low in both 30 min and 60 min (Fig. 7 K and L). We conclude that Stx2-KD delays maturation and acidification of phagosomes in macrophage cells.

Stx2-KD upregulates phagocytic uptake but attenuates lysosome-mediated clearance of IgG-opsonized E. coli

The antibacterial efficacy of macrophages hinges on their ability to internalize extracellular bacteria into phagosomes and subsequently deliver them to lysosomes for enzymatic degradation (Fairn and Grinstein, 2012). Given the increased phagocytosis of IgG-opsonized particles (Fig. 2) and their delayed maturation (Fig. 7), we sought to examine the impact of Stx2-KD on the uptake and clearance of opsonized *E. coli*. In line with our previous observations for OPB3 (Fig 3), Stx2-KD macrophages were more competent for trapping opsonized (mCherry expressing) *E. coli* (OPEC) (Fig. 8 A) and showed ~ 2 fold more surface-adherent OPEC over Control cells (Control: 5.7 OPEC/cell ; Stx2-KD: 11.5 OPEC/cell), when incubated for 30 min (Fig. 8 B). Extended incubation (1 hour) to allow sufficient internalization of OPEC and subsequent fluorescence imaging revealed that Stx2-KD cells engulfed OPEC ~ 2.2 more effectively (Control: 6 OPEC/cell ; Stx2-KD: 13.2 OPEC/cell) than Control cells (Fig. 8 C and D). Further, FACS analysis of cells incubated with OPEC for 1 hr unveiled that 89.1% of Stx2-KD cells were associated with OPEC compared to 51.2% for Control cells (Fig. 8 E). Moreover, the MFI, serving as an indicator of the degree of association of fluorescent particles per individual cell, was ~1.4 fold higher (Control: 2182, Stx2-KD: 3070) in Stx2-KD cells (Fig. 8 E). We then visualized the lysosomal delivery of internalized OPEC in Control and Stx2-KD cells in real time by time-lapse confocal microscopy (Fig. 8 F). Lysosomes were loaded with lysosome-specific fluorescent dye LysoSensor green that expectedly accumulated more in Stx2-KD cells and produced more intense green fluorescence (Fig. 8 F). Synchronised phagocytosis was then initiated after allowing OPEC to adhere macrophages for 20 min. With OPEC bearing red fluorescence, thus expected to produce yellow puncta upon delivery to green fluorescent lysosomes. We noticed appearance of yellow puncta from 20 min (arrow heads) in Control cells (Fig. 8F). Stx2-KD macrophages though internalized more OPEC and having more LysoSensor green stained lysosomes produced only a fewer puncta that also appeared at much later time point (at 40 min, arrow head). To assess how delayed lysosomal delivery impacts OPEC degradation, we incubated Control and Stx2-KD macrophages to internalize OPEC for 1 hr and allowed another 1 hr for phagosome maturation. Confocal imaging assessment showed majority of the internalized OPEC became fragmented in Control cells (Fig. 8 G). Stx2-KD macrophages though internalized higher number of OPEC; we noticed only a few fragmented structures (Fig. 8 G). Together, these data indicate that Stx2-KD macrophages though can uptake increased numbers of IgG-opsonized bacteria are unable to degrade them efficiently.

Discussion

In this study, we characterized the role of the SNARE protein Stx2 in macrophage phagocytosis for the first time. We found Stx2 is crucial for balancing phagocytic uptake of IgG-opsonized particles and their delivery to late endosome/lysosome compartments for degradation. We showed that Stx2 is distributed in multiple subcellular compartments, including the plasmalemma (both inner and outer leaflets), early endosomes, VAMP4-positive compartments (that includes primarily trans-Golgi and other organelles like sorting and recycling endosomes), and phagosomes in RAW 264.7 macrophage cells. Most of these cellular compartments are directly involved in the biogenesis of phagosomes (Flannagan et al., 2012; Shui et al., 2008). As such we found that Stx2 indeed controls various cellular processes that influence the course of phagocytosis. We observed that macrophages depleted for Stx2 (Stx2-KD) are more potent for the phagocytic uptake of IgG-opsonized particles. This enhanced uptake capacity could be attributed to both extracellular and intracellular events. Stx2-KD cells display elevated surface expression of FcRs, which facilitate actin-dependent remodelling of the plasmalemma upon engagement with IgG-opsonized particles (Swanson and Hoppe, 2004). Therefore, it is expected that the plasmalemma of Stx2-KD macrophages are more flexible in forming phagocytic cups that get hold on to the particles. In agreement with that we obtained increased formation of phagocytic cups and surface attached particles in Stx2-KD macrophages that successively internalized.

While the formation of phagocytic cups is one aspect of phagocytosis, their expansions in forming phagosomes and their maturation into phagolysosomes require regulated trafficking of membranes from intracellular compartments (Desjardins, 2003; Flannagan et al., 2012). Several lines of evidence validated exocytosis of early and recycling endosomes, ER, late endosomes and lysosomes at the phagocytic spots endorse phagocytosis (Desjardins, 2003; Flannagan et al., 2012). This process relies on organelle-associated v-/R-SNARE proteins (e.g., VAMPs), which mediate targeted delivery by forming complexes with target/plasmalemmal q-/t-SNAREs (e.g., Stxs and SNAPs), thus enabling membrane fusion. Inhibition of v-SNAREs (Bajno et al., 2000; Braun et al., 2004; Hackam et al., 1998) and SNARE regulatory proteins such as synaptotagmin VII (Czibener et al., 2006) have been shown to down regulate phagocytosis to various extents in macrophages. Based on our work we see that Stx2 is also a prominent plasmalemmal q-/-t-SNARE of macrophages (Hackam et al., 1996; Murray et al., 2005; Pagan et al., 2003). Our work also revealed that Stx2-KD significantly elevated the expansion of phagocytic cups that accompanied with enhanced delivery and acquisition of early endosomes and VAMP4-positive compartments. VAMP4 is known to be enriched within and control trafficking in between

trans-Golgi networks, which remain abstained from phagocytosis (Cebrian et al., 2011; Desjardins et al., 1994; Steegmaier et al., 1999). Our study could not detect trans-Golgi marker protein in phagosomes either. However, previous proteomic and western blot analysis on purified phagosomes confirmed abundant presence of VAMP4 in phagosomes (Rogers and Foster, 2007; Shui et al., 2008). Since VAMP4 trafficked to trans-Golgi through sorting and recycling endosomes (Tran et al., 2007), phagosomal delivery might be enhanced for these compartments in Stx2-KD macrophages. As we could not confirm this with specific markers, we kept this as 'VAMP4-positive post Golgi' compartments.

But how Stx2-KD can selectively upregulates trafficking of some compartments but inhibits others? Previous works on Stx2 disclosed its dual role in membrane fusions. For instance, in mucin secreting goblet cells (Wojnacki et al., 2023) and in rat kidney cells (Low et al., 2003), Stx2 pairs up with VAMP8 to mediate membrane fusions. Conversely, in zymogen-secreting pancreatic acinar cells (Dolai et al., 2018) and in insulin-secreting pancreatic beta cells (Kang et al., 2022; Zhu et al., 2017), Stx2 acts as an inhibitory (i)-SNARE by binding with VAMP8 and VAMP2, and thereby depriving other q-/t-SNAREs in forming fusion competent complex. One interesting observation that surfaced from our study is that Stx2-KD elevated trafficking of early endosomes and VAMP4-positive post Golgi compartments (all of them harbor Stx2), but diminished delivery of late endosomes and lysosomes (both deprived of Stx2) to the phagocytic cups and phagosomes. One plausible explanation is that Stx2 can restrict early endosomal VAMP2 (Sun et al., 2003) and VAMP4 from VAMP4-positive vesicles (Steegmaier et al., 1999) in forming complexes with other plasmalemmal and phagosomal Stxs (Hackam et al., 1996; Murray et al., 2005; Pagan et al., 2003). However, late endolysosomal VAMP7 and lysosomal VAMP8 could be the partners of Stx2, and thus, Stx2-KD impedes their incorporation into phagosomes, hindering their maturation into phagolysosomes. An earlier report on ER-resident v-/R-SNARE also demonstrated i-SNARE properties of Sec 22, where Sec22b inhibited Stx18 mediated ER membrane delivery to block phagocytosis in J774 macrophages (Hatsuzawa et al., 2009).

Another intriguing finding from our study is that Stx2-KD also increases cellular abundance of lysosomes. The most prominent factor that control lysosome biogenesis is the MiTF family of transcription factors including TFEB that lead the way by translocating inside the nucleus (Settembre et al., 2011). Our findings showed that Stx2-KD facilitates nuclear localization of TFEB at resting state. Multiple metabolic signalling pathways have been implicated in controlling nuclear translocation of TFEB (Puertollano et al., 2018). Mammalian target of rapamycin complex 1 (mTORC1) is notable one, and when activated inactivates mTORC1 confines TFEB outside the

nucleus. Activated mTORC1 also suppresses lysosome-mediated cellular catabolic process autophagy. The increment in basal autophagy in Stx2-KD macrophages suggests possible suppression of mTORC1 and thereby nuclear shuttling of TFEB (Settembre et al., 2012). Stx2-KD could also affect the vesicle trafficking underlying lysosome biogenesis (Yang and Wang, 2021). We also noticed increased nuclear enrichment of TFEB during the phagocytosis of opsonized particles. An earlier report directly linked TFEB activation by FcR during IgG-opsonized particle uptake (Gray et al., 2016). Since FcR expression is upregulated in Stx2-KD macrophages, this pathway could also be heightened in Stx2-KD macrophages. Additionally this could be a synergistic effect of mTORC1 inactivation, FcR activation and altered lysosomal trafficking. Further investigations are required to fully clarify these interesting findings. Additional works are also required to understand the mechanism for increased surface abundance of FcRs.

Nonetheless, our work unequivocally demonstrates critical involvement of Stx2 in macrophage phagocytosis. The opposing role of Stx2 in preventing excess uptake by restricting trafficking of non-lytic compartments and subsequently promoting lysosome directed clearance of engulfed particles is unique amongst all known macrophage SNAREs. This balancing act of Stx2 could have far reaching physiologic importance, considering adverse consequences of both hyperactive and timid macrophage phagocytosis in various human pathogenesis from autoimmunity, hemophagocytosis and neurodegeneration (Al-Samkari and Berliner, 2018; Butler et al., 2021; Kleinberger et al., 2014; Munoz et al., 2010). It would be interesting to see the status and functions of macrophage Stx2 in such pathogenesis and whether modulation of macrophage Stx2 level or activity could be effective in ameliorating pathobiology.

Figure legends

Figure 1. Stx2 is localized on inner/outer surface of plasmalemma, endosomal compartments and phagosomes of RAW 264.7 macrophages. (A) Representative confocal DIC (left) and immunofluorescence image (next to DIC) of endogenous Stx2 (green) and β-actin/ACTB (red) in RAW 264.7 cell. The boxed area is magnified and presented as individual and merged image for Stx2 and ACTB in the insets. Arrows indicate possible outer surface expressed Stx2. Scale bars, 10 and 5 µm (insets). DAPI (blue) indicates the nucleus. **(B and C)** Representative confocal DIC (top) and immunofluorescence images (below DIC) of non-permeabilized macrophages probed with either (B) anti-Stx2 and anti-ACTB antibodies or (C) anti-Stx2 antibody that pre-incubated with purified rat Stx2 (1 µg : 10 µg) and anti-ACTB antibodies to detect endogenous Stx2 (green) and ACTB (red). Higher magnification of the corresponding boxed area is shown in inset. DAPI (blue) shows the nucleus. Scale bars, 10 and 2 µm (insets). **(D)** FACS analysis of RAW 264.7 cells kept unlabeled (top), labeled with Alexa-488-conjugated anti-rabbit antibody (middle) or rabbit anti-Stx2/Alexa-488-conjugated anti-rabbit antibody (bottom). **(E)** Quantification of mean fluorescence intensity (MFI) of cells analyzed by FACS in (D). Values obtained from N=2 independent experiments. (**F and G)** Representative confocal DIC (left) and immunofluorescence images (next to DIC) of endogenous Stx2 (green) and (F) RAB5A (red) and (G) VAMP4 (red) in RAW 264.7 cells. The boxed areas are enlarged and shown as individual and merged images of corresponding proteins in the insets. Arrows point to the co-localized spots. Scale bars, 10 and 2 µm (insets). DAPI (blue) denotes the nucleus. **(H)** Representative confocal DIC (left) and immunofluorescence image (next to DIC) of 1 hr opsonized zymosan (OPZ) particle fed RAW 264.7 cells, probed for endogenous Stx2. Phagosomes containing OPZ particles are marked with white stars. Nucleus is labeled with DAPI (blue). Scale bars, 10 and 2 µm (insets). **(I)** Representative Western blots of Stx2 and LAMP1 in total cell lysates (TCL) and purified phagosomes (phago) from 1 hr opsonized OPB-0.8 fed Control and Stx2-KD RAW 264.7 macrophage cells. Protein molecular weight (in kilodalton: kDa) is shown on the left. Source data are available for this figure: Source Data F1.

Figure 2. Stx2 knockdown (Stx2-KD) augments phagocytosis of IgG-opsonized particles in macrophages. (A) Representative Western blot of total cell lysates (TCL) from RAW 264.7 cells (WT) and cells transduced with nonspecific scrambled (sc)-shRNA (Control) or shRNAs targeted to murine Stx2 (Stx2-KD), probed with antibodies to Stx2 or loading control β-actin (ACTB). The numbers on the left shows protein molecular weight (in kilodaltons: kDa). **(B)** Quantification of Stx2 band density values normalized to ACTB as means ± SEM (N = 3 independent

experiments). *P < 0.05, ns = not significant, determined by two-tailed unpaired Student's t test statistical analysis. **(C)** Representative confocal immunofluorescence image for Stx2 (green) in Control and Stx2-KD RAW 264.7 cells. DAPI (blue) shows the nucleus. Scale bars, 10 µm. **(D)** Representative confocal DIC (upper panel) and fluorescence images (bottom panel) generated by stacking 3 consecutive optical sections from Control or Stx2-KD RAW 264.7 macrophages incubated with IgG-opsonized zymosan red particles (OPZR) for 15, 30 and 60 min (left to right). Cells were additionally probed for Stx2 expression. DAPI (blue) represents the nucleus. Scale bars, 10 µm. **(E)** Quantification of the engulfed OPZR particles in Control and Stx2-KD RAW 264.7 macrophages as means ± SEM from at least 55 cells (N = 3 independent experiments). ***P < 0.0001 and ****P < 0.0001 estimated by two-tailed unpaired Student's t test statistical analysis. **(F)** Representative DIC confocal (upper panel) and maximum-intensity projection fluorescence images of Z-stacks (bottom panel) from Control and Stx2-KD RAW 264.7 cells incubated with IgG-opsonized red fluorescent beads (OPFB, 10 µm diameter; OPFB-10) for 30 and 60 min (left to right). ACTB (green) immunostaining marks the cell periphery. Nuclei were labeled with DAPI (blue). Scale bars, 10 µm. **(G)** Quantification values of the engulfed OPFB-10 particles in Control and Stx2-KD RAW 264.7 cells are shown by violin plot as means ± SEM obtained from at least 34 cells (N= 2 independent experiments). *P < 0.05 and **P < 0.05 assessed by two-tailed unpaired Student's t test statistical analysis. **(H)** Control and Stx2-KD RAW 264.7 cells alone (left panels) or in incubation with OPZR for 30 min (middle panels) or 60 min (right panels) were sorted by FACS to determine the degree of phagocytic uptake. **(I)** FACS analysis of Control or Stx2-KD cells without OPFB-10 (left panels) or in incubation with OPFB-10 for 60 min (right panel) to compare the phagocytic uptake. Source data are available for this figure: Source Data F2.

Figure 3. Stx2-KD promotes attachment of IgG-opsonised phagocytic particles by increased formation and expansion of phagocytic cups. (A) Representative scanning electron microscopy (SEM) images of Control (left panel) and Stx2-KD (right panel) RAW 264.7 cells incubated with IgG-opsonized latex beads (OPB, 3 µm diameter; OPB-3) for 5 min (top panel), 10 min (middle panel) and 30 min (bottom panel). Scale bars, 2 µm. Additional set of images are shown in **Fig. S3**. **(B)** Representative SEM images of Control (left panel) and Stx2-KD (right panel) RAW 264.7 macrophages magnified to show single attached OPB-3 and extension of plasmalemma around it (phagocytic cup). Scale bars, 2 µm. **(C)** Quantification of the surface attached OPB-3 per Control and Stx2-KD RAW 264.7 cells at the indicated time points expressed as means ± SEM (at least 11 Control cells and 8 Stx2-KD cells from N = 2 independent

experiments). ***P < 0.0001, ns = not significant, calculated by two-tailed unpaired Student's t test. **(D and E)** Quantification of the (D) mean surface area (μm^2) of individual OPB (at least 17 OPB from N=2 independent experiments) and (E) cumulative bead surface areas (μm^2) wrapped with plasmalemma at the indicated time points (at least 10 OPB from N=2 independent experiments). Values expressed as ± SEM. *P < 0.05, ***P < 0.0001, ****P < 0.0001, ns = not significant, calculated by two-tailed unpaired Student's t test. **(F)** Representative confocal DIC and stacked fluorescence images of Control (top panel) and Stx2-KD (bottom panel) macrophage cells incubated with OPFB-10 for 30 min and immunostained for ACTB (green). Boxed areas are magnified in the inset to show the accumulation of actin and the extension of phagocytic cups. DAPI (blue) is nucleus. Scale bars 10 and 5 µm (inset). **(G)** Quantitative analysis of the extension of phagocytic cups as mean OPFB surface area (μm^2) covered. Values presented as ± SEM. At least 20 cells from two independent experiments (N = 2) were analysed. **P < 0.01, derived by two-tailed unpaired Student's t test.

Figure 4: Stx2-KD elevates FcR expression and endomembrane trafficking for phagocytic cup expansion and phagosome biogenesis. (A) FACS analysis of Control (top panel) and Stx2-KD (bottom panel) RAW 264.7 macrophages kept unlabeled (left panel) or labeled with Alexa-568-conjugated anti-rat antibody (2^0Ab, middle panel) or with rat anti-FcRs/Alexa-568-conjugated anti-rat antibody (right). **(B)** Graph represents mean fluorescence intensities (MFI) of the FACS-analyzed samples for FcR expression. Values are from N=2 independent experiments for unlabeled and 2^0Ab labeled samples, and from N=3 independent experiments for FcR labeled samples. **(C)** Representative Western blots of total cell lysates (TCL) and purified phagosomes (phago) prepared from 30 min OPB (0.8 µm) fed Control and Stx2-KD RAW 264.7 cells, probed for RAB5A (early endosome protein), VAMP3 (recycling endosome SNARE), VAMP4 (trans-Golgi, sorting and recycling endosome SNARE), Golgin-160 (trans-Golgi), VAMP7 (late endosome SNARE) and VAMP8 (late endosome/lysosome SNARE). Tubulin acts as loading control for TCL and negative control for 'phago' fractions. A Ponceau S stained membrane shows uniform loading amongst TCL/phago. Protein molecular weight (in kilodalton: kDa) numbered in the left. **(D-I)** Quantitative analysis of the band density of (D) RAB5A, (E) VAMP3, (F) VAMP4, (G) Golgin-160, (H) VAMP7 and (I) VAMP8 in 'TCL' and 'phago' normalized to Ponceau S stained membrane. Values shown as ± SEM. *P < 0.05, **P < 0.01, ***P < 0.001 and ****P < 0.00001, judged by two-tailed unpaired Student's t test. **(J-M)** Representative confocal DIC (left panels) and fluorescence images (next to DIC) of Control (top panels) and stx2-KD (bottom panels) RAW 264.7 cells challenged with OPFB-10 for 30 min followed by immunostaining with (J) ACTB

(green) and RAB5A (cyan), (K) ACTB (cyan) and VAMP4 (green), (L) ACTB (cyan) and VAMP7 (green) and (M) ACTB (cyan) and VAMP8 (green). Nuclei made visible with DAPI (blue). Boxed regions of the images are enlarged in the inset panel (right). Scale bars 10 and 5 µm (inset). Source data are available for this figure: Source Data F3.

Figure 5: Stx2-KD boosts biogenesis of functional lysosomes macrophages. (A) FACS analysis of unstained (left panel) and LysoTracker Red DND-99 stained (right panel) Control (top panel) and Stx2-KD (bottom panel) RAW 264.7 cells. **(B)** Representative confocal DIC and fluorescence images of Control (top panel) and Stx2-KD (bottom panel) RAW 264.7 cells stained with LysoTracker Red DND-99. Boxed regions are magnified in inset. Nucleus (blue) stained with Hoechst. Scale bars, 10 µm, 5 µm (inset). **(C)** Quantification of LysoTracker Red intensity (in arbitrary unit: A.U.) from individual Control and Stx2-KD RAW 264.7 cells presented as violin plot. Values are in ± SEM (at least 93 cells from N = 3 independent experiments). ***P < 0.0001, assessed by two-tailed unpaired Student's t test. **(D)** Representative confocal DIC and fluorescence images of Control (top panel) and Stx2-KD (bottom panel) RAW 264.7 macrophages immunostained for LAMP1 (red). Boxed areas enlarged in inset. Nuclei (blue) labeled with DAPI. Scale bars, 10 µm, 5 µm (inset). **(E)** Quantification of the LAMP1 fluorescence intensity (in A.U.) from individual Control and Stx2-KD RAW 264.7 cells shown as violin plot. Values expressed as ± SEM (at least 50 cells from N = 3 independent experiments). ***P < 0.0001, determined by two-tailed unpaired Student's t test. **(F)** Representative Western blots show expression of LAMP1 and loading control ACTB in total cell lysates (TCL) from Control and Stx2-KD macrophages. Protein molecular weight (in kilodaltons: kDa) is numbered in left. **(G)** Quantification of LAMP1 band intensity normalized to ACTB loading control. Values expressed as means ± SEM (N = 3 independent experiments). **P < 0.001, calculated by two-tailed unpaired Student's t test. **(H)** Representative confocal DIC and immunofluorescence merged images (next to DIC) of Control (top panel) and Stx2-KD (bottom panel) RAW 264.7 macrophages probed for lysosomal hydrolases cathepsin L (CTSL: red), cathepsin B (CTSB: green) and cathepsin D (CTSD: cyan). Boxed regions are magnified and split into separate channels in the inset. Scale bars 10 and 2 µm (inset). **(I)** Quantification of indicated cathepsin fluorescence intensity from individual Control and Stx2-KD cells (in A.U.). Values displayed as ± SEM (at least 56 cells from N = 3 independent experiments). *P < 0.05 and ***P < 0.001, calculated by two-tailed unpaired Student's t test. **(J)** Representative Western blots of TCL from Control and Stx2-KD RAW 264.7 macrophages probed for CTSL, CTSB, CTSD and loading control ACTB. Protein molecular weight (in kDa) numbered in left. **(K-M)** Quantification of band density for (K) CTSL, (L) CTSB

and (M) CTSD normalized to ACTB. Values are in ± SEM (N = 3 independent experiments). **P < 0.01 and ***P < 0.001, determined by two-tailed unpaired Student's t test. determined by two-tailed unpaired Student's t test. **(N)** Representative Western blots of TCL from Control and Stx2-KD RAW 264.7 macrophages probed for LC3-I/II, SQSTM1/p62 and loading control ACTB. Protein molecular weight (in kDa) shown in left. **(O and P)** Quantification of band density for (O) LC3-II/I and (P) SQSTM1/p62 normalized to ACTB. Values depicted as ± SEM. (N = 3 independent experiments). **P < 0.01, calculated by two-tailed unpaired Student's t test. Source data are available for this figure: Source Data F4.

Figure 6. Stx2-KD augments nuclear translocation of transcription factor EB (TFEB). (A) Representative Western blots of total cell lysates (TCL) from Control and Stx2-KD macrophages probed for TFEB. **(B)** Quantification of band densities normalized to ACTB. Values expressed as ± SEM from N = 3 independent experiments. ns = not significant, estimated by two-tailed unpaired Student's t test. **(C)** Representative confocal DIC (left panels) and fluorescence images (next to DIC) of Control (top panels) and stx2-KD (bottom panels) RAW 264.7 macrophages immunostained for lysosome marker protein LAMP1 (purple) and master transcription factor for lysosome biogenesis protein TFEB (green). White circle marks the periphery of nuclei. Boxed sections of the images are magnified in the inset panel (right). Nuclei labeled with DAPI (shown as pseudo red). Scale bars 10 and 5 µm (inset). **(D)** Representative Western blots of TCL from Control and Stx2-KD macrophages kept unchallenged (0 min) or challenged with OPB-3 for 15 to 60 min and probed for LAMP1, CTSL, CTSB and loading control ACTB. **(E-G)** Quantification of the band density of (E) LAMP1, (F) CTSL and (G) CTSB normalized to ACTB. All values are means ± SEM. *P < 0.05, **P < 0.01 and ns = not significant, obtained by two-tailed unpaired Student's t test statistical analysis. **(H)** Representative confocal DIC (left panels) and fluorescence images (next to DIC) of Control (top panels) and stx2-KD (bottom panels) RAW 264.7 macrophages incubated with OPB-3 for 30 min followed by immunostaining with lysosome marker protein LAMP1 (purple) and TFEB protein (green). White circle shows the nuclear periphery. Boxed sections of the images are enlarged in the inset panel (right). Nuclei visualized with DAPI (shown as pseudo red). Scale bars 10 and 5 µm (inset). Source data are available for this figure: Source Data F5.

Figure 7. Stx2-KD impairs phagosome acquisition of lysosomal proteins and phagosome acidification. (A) Representative confocal DIC (top panel) and fluorescence images (middle panel) of OPZ fed (15 to 60 min: left to right) Control and stx2-KD RAW 264.7 macrophages

immunostained for lysosome marker protein LAMP1 (red). White stars show the OPZ-containing phagosomes. Boxed regions encompassing single phagosome is magnified in the inset panel (bottom). DAPI (blue) marks the nuclei. Scale bars 10 and 2 µm (inset). **(B)** Quantification of the phagosomal LAMP1 fluorescence intensity (in arbitrary units: A.U.) in Control and Stx2-KD RAW 264.7 cells. Values presented as ± SEM (Control: 19 phago and Stx2-KD: 42 phago from N = 3 independent experiments). ****P < 0.00001, determined by two-tailed unpaired Student's t test. **(C)** Representative confocal DIC and fluorescence images of 60 min OPZ fed Control (top panel) and Stx2-KD (bottom panel) RAW 264.7 macrophages immunostained for lysosomal hydrolases cathepsin L (CTSL: red), cathepsin B (CTSB: green) and cathepsin D (CTSD: cyan). Individual phagosomes correspond to the boxed areas are magnified and shown as separate channels in inset. Nuclei (blue) were labeled with DAPI. Scale bars 10 and 2 µm (inset). **(D)** Quantification of the phagosomal fluorescence intensity for CTSL, CTSB and CTSD in A.U. in Control and Stx2-KD RAW 264.7 cells. Values estimated as ± SEM (at least 43 phagosomes from N = 3 independent experiments). *P < 0.05 and ****P < 0.00001 obtained from two-tailed unpaired Student's t test. **(E)** Representative Western blots of total cell lysates (TCL) and purified phagosomes (phago) from 1.5 hr opsonized OPB-0.8 fed Control and Stx2-KD RAW 264.7 macrophages probed for LAMP1, CTSL, CTSB, CTSD and ATP6V1A (v-ATPase subunit). Tubulin is used as loading control for TCL and negative control for 'phago'. Representative Ponceau S stained membrane shows uniform loading amongst TCL and phago. Protein molecular weight (in kilodalton: kDa) shown in left. **(F-J)** Quantification of the band density of (F) LAMP1, (G) CTSL, (H) CTSB, (I) CTSD and (J) ATP6V1 in 'TCL' and 'phago' normalized to Ponceau S stained membrane. Values shown as ± SEM. **P < 0.01, ***P < 0.001 and ****P < 0.00001 calculated from two-tailed unpaired Student's t test. **(K)** Representative confocal DIC (left panel) and fluorescence images (right panel) of 30 and 60 min (top and bottom panel respectively) pHrodo Red Zymosan (pHRZ) particle fed Control and Stx2-KD RAW 264.7 macrophages. DAPI (blue) used to visualize nuclei. Scale bars 10 µm. **(L)**. Quantification of pHRZ particle fluorescence intensity stated as ± SEM (30 min: Control/16 particles, Stx2-KD: 33 particles; 60 min: Control/46 particles, Stx2-KD: 27 particles from N = 2 independent experiments). ****P < 0.00001 estimated by two-tailed unpaired Student's t test.

Figure 8. Increased phagocytosis and defective clearance of E. coli in Stx2-KD macrophages. **(A)** Representative SEM images of Control and Stx2-KD RAW 264.7 macrophages challenged with IgG-opsonized mCherry-expressing *E. coli* (OPEC) for 30 min. **(B)** Quantification of the surface adherent OPEC per macrophage shown as ± SEM (at least 10

macrophages from N = 2 independent experiments). ***P < 0.0001, derived by two-tailed unpaired Student's t test. **(C)** Representative confocal DIC and fluorescence images of Control and Stx2-KD RAW 264.7 macrophages challenged with OPEC for 1 hr. DAPI (blue) denotes the nuclei. Scale bars 10 µm. **(D)** Quantification of engulfed OPEC per macrophage cell is presented as **±** SEM (at least 105 cells from N = 3 independent experiments). ****P < 0.00001, estimated by two-tailed unpaired Student's t test. **(E)** FACS analyses of OPEC phagocytosis by Control (top panel) and Stx2-KD (bottom panel) RAW 264.7 macrophages. **(F)** Representative time-lapse spinning-disk confocal fluorescence images of the Control (top panel) and Stx2-KD (bottom panel) RAW 264.7 macrophages challenged for OPEC phagocytosis in presence of LysoSensor Green after 20 min of attachment (denoted as 0'). Stacked images from the indicated time points (top right corner) are shown. OPEC fusing with lysosomes (yellow puncta) indicated with arrowheads. DAPI (blue) was used to visualize nuclei. Scale bars 10 µm. The sequence of fluorescence images with corresponding DIC images are shown in **Fig. S5**. **(G)** Representative confocal DIC and fluorescence stacked images of Control (top panel) and Stx2-KD (bottom panel) macrophages challenged with OPEC for 2 hr (1 hr uptake + 1 hr maturation) and immunostained for ACTB (green). Nuclei were stained with DAPI (blue). Boxed areas are magnified in the inset. Arrows show the fragmented OPEC. Scale bars, 10 µm, 5 µm (inset).

Materials and methods

Antibodies and reagents

Antibodies used for this study are enlisted in Table 1 along with their application and dilution. Reagents used are mentioned in Table 2. Any other materials unless specified were from Sigma-Aldrich.

Table 1. Antibodies

Antibody	Source/Identifier	Application/Dilution
Primary antibodies		
Anti-Syntaxin2, Rabbit polyclonal	Synaptic Systems (Cat# 110123, RRID:AB_887849)	ICC; 1:200
Anti-Syntaxin2, Rabbit polyclonal	Thermo Fisher Scientific (Cat# PA5-87903, RRID:AB_2804493)	WB; 1:1000
Anti-Syntaxin2, Mouse polyclonal	R and D Systems (Cat# AF2568, RRID:AB_2302866)	ICC; 1:200
Anti-VAMP3, Rabbit polyclonal	Proteintech (Cat# 10702-1-AP, RRID:AB_2212628)	WB; 1:2000 ICC; 1:200
Anti-VAMP4, Rabbit polyclonal	Thermo Fisher Scientific (Cat# PA1-768, RRID:AB_2212790)	WB; 1:500 ICC; 1:100
Anti-VAMP7, Rabbit polyclonal	Thermo Fisher Scientific (Cat# PA5-116892, RRID:AB_2901522)	WB; 1:500 ICC; 1:100
Anti-VAMP8, Rabbit polyclonal	Proteintech (Cat# 15546-1-AP, RRID:AB_2878150)	WB; 1:1000 ICC;
Anti-Rab5A, Mouse monoclonal	Cell Signaling Technology (Cat# 46449, RRID:AB_2799303)	ICC; 1:100
Anti-LAMP1/CD107a, Rat monoclonal	Thermo Fisher Scientific (Cat# 14-1071-81, RRID:AB_657532)	ICC; 1:500
Anti-LAMP1/CD107a, Goat monoclonal	R and D Systems (Cat# AF4320, RRID:AB_2296826)	WB; 1:1000
Anti-Cathepsin L (CTSL), Goat polyclonal	R and D Systems (Cat# AF1515, RRID:AB_2087690)	WB; 1:1000 ICC; 1:100

Anti-Cathepsin B (CTSB), Rabbit monoclonal	Cell Signaling Technology (Cat# 31718, RRID:AB_2687580)	WB; 1:1000 ICC; 1:100
Anti-Cathepsin D (CTSD), Rabbit polyclonal	Proteintech (Cat# 21327-1-AP, RRID:AB_10733646)	WB; 1:1000
Anti-Cathepsin D (CTSD), Mouse monoclonal	Cloud-Clone Corporation (Cat# MAB280Hu22, RRID: Not available)	ICC; 1:100
Anti-Lipopolysaccharide (LPS), Mouse monoclonal	Cloud-Clone Corporation (Cat# MAB526Ge24, RRID: Not available)	ICC; 1:500
Anti-ATP6V1A (E5N9E), Rabbit monoclonal	Cell Signaling Technology (Cat# 39517, RRID:AB_3083783)	WB; 1:1000
Anti-LC3A/B, Rabbit monoclonal	Cell Signaling Technology (Cat# 12741, RRID:AB_2617131)	WB; 1:500
Anti-SQSTM1/p62, Rabbit monoclonal	Cell Signaling Technology (Cat# 39749, RRID:AB_2799160)	WB; 1:1000
Anti-TFEB, Rabbit polyclonal	Cell Signaling Technology (Cat# 4240, RRID:AB_11220225	ICC; 1:100
Anti-Tubulin, Rabbit polyclonal	Cell Signaling Technology (Cat# 3873, RRID:AB_1904178)	WB; 1:2000
Anti-Actin, Rabbit polyclonal	BioBharti (Cat# BB-AB0025, RRID: Not available)	WB; 1:4000
Anti-Actin, Mouse monoclonal	Cell Signaling Technology (Cat# 3700, RRID:AB_2242334)	ICC; 1:600
Anti-CD16/CD32 (Fcγ), Rat Monoclonal	Thermo Fisher Scientific (Cat# 14-0161-82, RRID:AB_467133)	Flow; 1:100
Secondary antibodies		
Anti-Mouse Donkey IgG(H+L), Alexa Fluor 488-conjugated	Jackson ImmunoResearch (Cat# 715-545-150, RRID:AB_167505)	ICC; 1:800
Anti-Rabbit Donkey IgG(H+L), Alexa Fluor 488-conjugated	Jackson ImmunoResearch (Cat# 711-545-152,	ICC; 1:800

	RRID:AB_168465)	
Anti-Rabbit Goat IgG(H+L), Alexa Fluor 594-conjugated	Jackson ImmunoResearch (Cat# 111-585-003, RRID:AB_163359)	ICC; 1:800
Anti-Goat Donkey IgG(H+L), Alexa Fluor 594-conjugated	Jackson ImmunoResearch (Cat# 705-585-003, RRID:AB_156820)	ICC; 1:800
Anti-rat Goat IgG(H+L), Alexa Fluor 488-conjugated	Thermo Fisher Scientific (Cat# A-11006, RRID:AB_2534074)	ICC; 1:800
Anti-rat Goat IgG(H+L), Alexa Fluor 568-conjugated	Thermo Fisher Scientific (Cat# A-11077, RRID:AB_2534121)	ICC; 1:800
Anti-rabbit Goat IgG(H+L), Alexa Fluor 488-conjugated	Thermo Fisher Scientific Cat# A-11034, RRID:AB_2576217)	ICC; 1:800
Anti-mouse Goat IgG(H+L), Alexa Fluor 488-conjugated	Thermo Fisher Scientific (Cat# A-11004, RRID:AB_2534072)	ICC; 1:800
Anti-Rabbit Goat IgG (H+L) Alexa Fluor Plus 647-conjugated	Thermo Fisher Scientific (Cat# A32733), RRID:AB_2633282	ICC; 1:800
Anti-Rabbit Goat IgG (H+L), HRP-conjugated	Thermo Fisher Scientific (Cat# 31460, RRID:AB_228341)	WB; 1:5000
Anti-Mouse Rabbit IgG, HRP-conjugated	Millipore (Cat# AP160P, RRID:AB_92531)	WB; 1:5000
Anti-Goat Rabbit IgG, HRP conjugate	(Millipore Cat# AP106P, RRID:AB_92411)	WB; 1:5000

Table 2. Reagents

Reagent	**Source**	**Identifier**
Syntaxin 2 shRNA (m) Lentiviral Particles	Santa Cruz Biotechnology	Cat# sc-41327-V
Control shRNA Lentiviral Particles-A	Santa Cruz Biotechnology	Cat# sc-108080
Polybrene Infection / Transfection Reagent	Sigma-Aldrich	Cat# TR-1003
Puromycin dihydrochloride	Sigma-Aldrich	Cat# P7255
Human IgG	Sigma-Aldrich	Cat# I4506

Zymosan A, unlabeled	Thermo Fisher Scientific	Cat# Z2849
Zymosan A, Alexa Fluor™ 594 conjugated	Thermo Fisher Scientific	Cat# Z23374
FluoSpheres™ Polystyrene Microspheres, 10 µm, red fluorescent (580/605)	Thermo Fisher Scientific	Cat# F8834
pHrodo™ Red Zymosan BioParticles™	Thermo Fisher Scientific	Cat# P35364
LysoTracker™ Red DND-99	Thermo Fisher Scientific	Cat# L7528
LysoSensor™ Green DND-189	Thermo Fisher Scientific	Cat# L7535
ProLong™ Diamond Antifade Mountant with DAPI	Thermo Fisher Scientific	Cat# P36962
Hoechst 34580	Thermo Fisher Scientific	Cat# H21486
Latex beads, deep blue dyed 0.80 µm average diameter	Sigma-Aldrich	Cat# L1398
Latex beads, polystyrene 3.0 µm mean particle size	Sigma-Aldrich	Cat# LB30
Syntaxin2 protein	Synaptic Systems	Cat# 110-2P
RIPA Lysis Buffer System	Santa Cruz Biotechnology	Cat# sc-24948
Protease inhibitor cocktail	Sigma-Aldrich	Cat# P8340
Ponceau S Staining Solution	Thermo Fisher Scientific	Cat# A40000279
Nitrocellulose membrane, 0.2 µm	Bio-Rad	Cat# 1620112
SuperSignal™ West Pico PLUS Chemiluminescent Substrate	Thermo Fisher Scientific	Cat# 34577
DMEM	Thermo Fisher Scientific	Cat# 12100061
Fetal Bovine Serum (FBS)	Avantor	Cat# 97068-085
DMSO, Anhydrous	Thermo Fisher Scientific	Cat# D12345
Penicillin-streptomycin	Thermo Fisher Scientific	Cat# 15140122
L-Glutamine	Thermo Fisher Scientific	Cat# 25030081

RAW 264.7 cell culture and generation of stable Stx2 knockdown cell line

Authentic murine RAW 264.7 macrophage cells (#TIB-71; ATCC) were grown at 37°C under 5% CO_2 in Dulbecco's Modified Eagle's Medium (DMEM) supplemented with 10% fetal bovine serum

(FBS), 100 U/ml of penicillin-streptomycin, and 2 mM L-glutamine. Overnight cultures of passage 5 cells at approximately 50% confluency were mixed with 5 µg/mL polybrene one hour prior to infection with lentiviral particles (MOI: 5) expressing either non-specific scrambled (sc) shRNA to obtain Control cells or mouse Stx2-shRNAs to obtain knockdown cells (Stx2-KD), following the manufacturer's guidelines. Virus/polybrene-containing media were replaced with fresh DMEM 12 hours post-infection, and cells were allowed to grow for another 24 hours before seeding onto 100 mm dishes. Puromycin (5 µg/mL) was added to the culture medium to select for transduced colonies, which were isolated individually using cloning cylinders (Tr1004, Millipore) and maintained under selection pressure. The expression level of Stx2 was verified by western blot, and the chosen Control and Stx2-KD clones were propagated, frozen, and considered as a new "Passage 1". All experiments were conducted using cells below 10 passages to minimize potential alterations due to prolonged culturing.

Phagocytosis assay of opsonized particles

Phagocytosis assays were performed according to published methodologies with minor adaptations (Czibener et al., 2006; Huang et al., 2009; Wong et al., 2017). Briefly, Control or Stx2-KD RAW 264.7 cells ($1X10^6$ each) were seeded overnight on 22 mm glass coverslips (#CLS284522, Corning) placed within 6-well culture plates (#980010/Tarsons). For zymosan particle phagocytosis, particles (unlabeled and Alexa-594 labeled: zymosan red) were reconstituted in DMEM (10^8/ml) and opsonized overnight at 4^0C by incubating with 1mg/mL human IgG. Opsonized unlabeled zymosan (OPZ) and zymosan red (OPZR) particles were combined with the culture at 15:1 ratio (particles: cell). Zymosans labeled with pHrodo red (pHRZ) were reconstituted freshly and added to the culture at 15:1 ratio (particles: cell) without opsonization. For latex/polystyrene bead phagocytosis, both nonfluorescent and fluorescent beads of variable diameters (0.8, 2.0, 3.0 and 10 µm) were resuspended in PBS and opsonized overnight with human IgG (1 mg/mL) at 4^0C. Opsonized nonfluorescent (OPB, 0.8 µm and OPB, 3.0 µm) and fluorescent (OPFB, 2.0 µm and OPFB, 10 µm) beads were washed twice with PBS (5000 rpm, 5 min) and added to the culture at 15:1 (beads: cell). After addition of relevant beads, plates were immediately centrifuged at 1,000 rpm for 1 min (Hermle Z366K fitted with 221.16 rotor) to settle the phagocytic objects uniformly on the cells. Plates were quickly placed at 37^0C in a 5% CO_2 incubator to initiate synchronized phagocytosis. Phagocytosis events were terminated at different time points (as indicated in the legends) by washing the cells with ice-cold PBS. Phagocytic uptake and phagosome maturation were analyzed by fluorescence imaging, flow

cytometry, fractionation, and scanning electron microscopy (SEM), where applicable, as stated below.

E. coli phagocytosis and degradation assay

An E. coli (BL21-DE3) strain expressing red fluorescent protein mCherry (E. coli-mCherry) was generated for imaging based assay of phagocytosis and degradation. Bacteria were grown to mid-log phase (OD600 0.5-1.0) in Luria broth, washed twice in PBS (2,000 × g, 5 min) and brought into suspension by vortexing. 100 µL of E. coli suspension was opsonized (OPEC) with 10 µL of anti-LPS antibody for 1 hr in RT followed by PBS wash (2,000 × g, 5 min) and resuspension in DMEM. A low speed centrifugation (300 × g, 5 min) was applied to remove clumped E. coli. Numbers of E. coli in suspension were counted and used at 1:50 (cell: bacteria) to infect Control and Stx2-KD RAW 264.7 cells grown overnight on 22 mm glass coverslips placed within 6-well plates. Plates were centrifuged immediately at 1,000 rpm for 1 min and placed within a 37^0C incubator. Phagocytosis was halted at 1 hr or 2 hr by wash with ice-cold PBS followed by fixation (2% PFA in PBS) and mounting. Coverslips were imaged using a confocal fluorescence microscope to assess the number of engulfed bacteria and their morphology.

Immunostaining and confocal microscopy

Cells grown on coverslips were washed in PBS and fixed in 2% PFA for 10 min at room temperature (RT). Cells were then permeabilized with 0.1% Triton X-100 in PBS for 5 minutes, washed in PBS and blocked with 0.2% gelatin for 5-minute at RT. Desired primary antibodies (diluted in 0.2% gelatin) were then added to the cells for 1 hour, washed in PBS, followed by 1 hr incubation with appropriate secondary antibodies conjugated to Alexa Fluor 488, Alexa Fluor 594 or Alexa Fluor 647 (antibody dilutions are stated in “antibodies and reagents” section). After a wash in PBS, coverslips were mounted with a mountant containing DAPI (nuclear stain). Cells intended to be kept impermeable for inside-outside labeling were processed without permeabilization. Z-series confocal images were captured at a 0.34 µm interval with a Leica SP8 confocal platform equipped with a 63X/1.4 NA oil immersion objective (Zeiss) with appropriate laser excitation and emission filters. Images were deconvoluted using Leica Lightning software. Fluorescence signal were quantified using Zen (Carl Zeiss) software.

Live cell confocal microscopy

For LysoTracker imaging, RAW 264.7 cells were cultured on 35-mm glass-bottom petri dish and incubated with LysoTracker Red DND-99 (50 nM) and nuclear stain Hoechst 33342 (1µg/mL) for 30 min in a 5% CO_2 incubator at 37°C. Cells were then washed and kept in PBS containing LysoTracker Red DND-99 (50 nM) and Hoechst 33342 (1µg/mL) and imaged immediately using a Leica SP8 confocal microscope as stated above. For live imaging of bacterial phagocytosis, Stx2-KD RAW 264.7 cells were grown on glass-bottom petri dish and loaded with LysoSensor Green (500 nM in DMEM). OPEC were added to the cells (1:50, cell: bacteria) and allowed to adhere for 15 min, followed by washing with PBS. Fresh DMEM with LysoSensor Green was added and samples were placed within a CO_2 (5%) and temperature (37^0C) controlled stage top incubator (Tokai Hit). Image stacks were recorded for 1 hr at 5 min interval using an Olympus SpinSR confocal microscope equipped with Yokogawa CSU-W1 scan head and a 60X/1.42 NA oil immersion objective (Olympus). Laser excitation and emission filters were 488 nm (ex) 525/50 nm (em) for green fluorescence, 568 nm (ex) 617/ 73 nm (em) for red fluorescence and 360 nm (ex) 525/50 nm (em).

Flow cytometry (FACS)

All FACS analyses were performed by a BD LSR Fortessa flow cytometer using appropriate filter set up and analyzed with BD FACSDiva software. Lysotracker staining and FACS analyses were performed following a published methodology (Zhang et al., 2022) with minor adjustments. Control and Stx2-KD cells were trypsinized and brought in to suspension (1.2 X 10^6cells/mL) in 10% FBS containing DMEM followed by 15 min incubation with 50 nM Lysotracker Red DND-99 in a CO_2 incubator. Cells were then pelleted at 300×g for 3min, resuspended in 50 nM Lysotracker Red DND-99 containing ice-cold 1XPBS and analyzed immediately. For surface staining of Stx2 and FcRs, 1.2 X 10^6 cells were fixed in 1% PFA (in PBS) for 5min followed by 0.2% gelatin blocking for 15 min at RT. Cells were then incubated with anti-rabbit Stx2 (1:200) and anti-rat FcRs/CD11b/c (1:200) antibody (Czibener et al., 2006) for 1 hr at 4^0C followed by PBS wash (3 times, each 5 mins) and subsequent incubation with anti-rabbit Alexa-568(1:800) and anti-rat Alexa-488(1:800) for 1 hr at 4^0C. Cell were again washed with PBS (3 times, each 5 mins) and finally resuspended in 1 mL 1xPBS before FACS analyses. For the detection of phagocytosis, cells were washed with ice-cold PBS to halt uptake of fluorescent particles (OPFB-2, OPZR, OPFB-10 and OPEC). Cells were then trypsinized and brought in to suspension in ice-

cold PBS and spun down at 300 g for3 min at 4^0C to remove aggregates. Pellets were then resuspended in 0.8 mL ice-cold PBS (10^6/mL) and subjected to FACS analyses.

SEM

Monolayers of RAW 264.7 cells on glass coverslips were incubated with OPB (3 µm; 1: 15, cell: OPB) or OPEC (1: 100, cell: bacteria) and arrested for phagocytosis at different time as elaborated earlier. Cells were then fixed in 2.5% glutaraldehyde (in PBS, pH 7.4) for 1 hr at 4^0C. After washing with PBS twice, cells were osmicated for 20 min in 1% (vol/vol) aqueous osmium tetroxide at RT. Cells were then washed with PBS, followed by dH_2O and dehydrated by 5 min sequential incubations in 30, 50, 60, 80 and 100% ethanol. Samples were further dried overnight in a vacuum desiccator and imaged using a Zeiss Supra 55VP scanning electron microscope operating at 5.2 kV.

Purification of phagosomes

Phagosomes were purified by adopting the revised methodology of Desjardins et al (Descoteaux, 2009; Desjardins et al., 1994). Briefly, Control or Stx2-KD cells were grown on 150 mm Petri dishes (CLS430599, Corning) to obtain ~ 4 X 10^7 cells for each condition. Cells were then incubated with OPB (0.8 µm, blue-dyed: OPB-0.8) at a ratio of 50:1 (beads: cell) for 30 min to 1 hr. Subsequently, the cells were washed with warm DMEM to eliminate unbound OPB-0.8 and either approached for purification immediately (for 30 min OPB-0.8 incubated cells to obtain nascent phagosomes) or allowed to mature for another 30 min (for 1 hr OPB-0.8 incubated cells). For phagosome isolation, cells were then washed and scrapped in ice-cold PBS, and pelleted at 1200 rpm at 4°C. Pellets were washed with 10 mL ice-cold homogenization buffer (HB: 8.55% sucrose, 3 mM imidazole, 2X PIC, pH 7.4) for 5 minutes and pelleted at 1200 rpm. Pellets were brought to suspension in 1 mL HB with 2X PIC and passed through a 30-G needle (fitted in a 1 mL syringe) until □90% of cells were broken, as confirmed by phase microscopy. The homogenates were clarified at 1200 rpm for 5 minutes, and supernatants enriched with OPB-0.8 containing phagosomes were mixed with an equal volume of 62% sucrose. This mixture was layered over 3 mL of 62% sucrose, followed by sequential topping with 2 mL each of 35, 25, and 10% sucrose (all prepared in 3 mM imidazole, pH 7.4) in SW40 tubes (344060, Beckman). The samples were then centrifuged at 100,000 g for 1 hr at 4°C using a SW40Ti rotor (Beckman). Phagosomes were recovered from the interface of 10 and 25% sucrose (Fig. S4) using a Pasteur pipette, washed with 12 mL ice-cold PBS, and harvested at 40,000 g.

Western blotting

RAW 264.7 ells or purified phagosomes were lysed in ice-cold RIPA buffer with a protease inhibitor cocktail (PIC, 1X). Samples were then sonicated using a sonicator (Sartorius) and separated from insoluble debris at 10,000g for 10 min at 4°C. Protein concentration was estimated using modified Lauri method and brought to similar level by adding RIPA buffer containing PIC. Lysates were then boiled in Laemmli buffer, resolved by 10-12% SDS–PAGE and transferred to nitrocellulose membranes. Non-specific binding sites were blocked in 5% skim milk dissolved in TBST (TBS with 0.1% Tween-20) for 1 hr at RT and then incubated with primary antibodies for 12 h at 4^0C (see “antibodies and reagents” table for specific antibody dilutions). After washing with TBST, membranes were incubated with suitable HRP-conjugated secondary antibodies in 5% skim milk/TBST for 1 hr at RT. Membranes were then washed in TBST, developed with ECL reagent and documented using a ChemiDoc imaging system (Bio-Rad). Densitometry analysis of the bands was accomplished using ImageJ 1.54i software (NIH, USA).

Statistical analyses

Quantification of data was analyzed to verify statistical significance using unpaired Student’s t-test. Graphs were prepared using GraphPad Prism Software (GraphPad Prism version 8.3.1 for Windows; GraphPad Software, www.graphpad.com).

Online supplemental material

Fig. S1 shows the immunofluorescence images of Stx2/VAMP7 and Stx2/LAMP1, in continuation to **Fig. 1 F and G** images. **Fig. S2** shows the screening of Stx2-KD RAW 264.7 clones and the effect of Stx2-KD on OPFB-2.0 phagocytosis. Related to **Fig. 2**. **Fig. S3** shows another set of SEM images in addition to **Fig. 3 A**. **Fig. S4** shows the phagosome purification scheme and the OPB-0.8 engulfed cells and the phagosome fraction (blue) in the sucrose gradient tube. **Fig. S5** shows the time course images of **Fig. 8F**, along with the corresponding DIC images.

Data availability

Uncropped Western blot images in the main and supplemental figures are provided in source data files. All other data that supports the results of this study are available from the corresponding author (subhankar.dolai@gmail.com) upon reasonable request.

Acknowledgements

This work was supported by the Science and Engineering Research Board-State University Research Excellence (SERB-SURE) research grant No: SUR/2022/001269) and Department of Biotechnology (DBT) Ramalingaswami Re-entry Fellowship cum research grant No: BT/RLF/Re-entry/07/2019 awarded to S. Dolai, and Indian Council of Medical Research (ICMR) research grant No: 6/9-7(318)/2023-ECD-II awarded to R. Datta.

The authors thank IISER Kolkata core instrument facility staffs: Mr. Tamal Ghosh for FACS, Mr. Kashinath Sahu for SEM and Ms. Shreya Ghosh for Spinning Disk imaging. Authors also thank R. Datta lab members for their technical support. Authors also thank Prof. Mohit Prasad for LysoSensor Green and Dr. Arnab Gupta for anti-TFEB and Alexa Fluor 647-conjugated antibodies. Authors are also grateful to Prof. Jayasri Das Sarma and Dr. Sankar Maiti for their valuable suggestions on various occasions.

Author contribution

S. Samanta: Methodology, Investigation, Visualization, Data analysis, Validation, Reviewing and Editing. **A. Nandi:** Investigation, Visualization, Methodology, Reviewing and Editing. **R. Datta:** Laboratory set up, Supervision, Resources, Funding acquisition, Methodology, Writing, Reviewing and Editing. **S. Dolai:** Supervision, Funding acquisition, Conceptualization, Resources, Methodology, Investigation, Visualization, Data analysis, Writing, Reviewing, Editing and Validation.

Disclosures

The authors declare no conflicts and no competing financial interests.

References

Aderem, A., and D.M. Underhill. 1999. Mechanisms of phagocytosis in macrophages. *Annual review of immunology*. 17:593-623.

Al-Samkari, H., and N. Berliner. 2018. Hemophagocytic Lymphohistiocytosis. *Annual review of pathology*. 13:27-49.

Arandjelovic, S., and K.S. Ravichandran. 2015. Phagocytosis of apoptotic cells in homeostasis. *Nature immunology*. 16:907-917.

Bajno, L., X.R. Peng, A.D. Schreiber, H.P. Moore, W.S. Trimble, and S. Grinstein. 2000. Focal exocytosis of VAMP3-containing vesicles at sites of phagosome formation. *The Journal of cell biology*. 149:697-706.

Becken, U., A. Jeschke, K. Veltman, and A. Haas. 2010. Cell-free fusion of bacteria-containing phagosomes with endocytic compartments. *Proceedings of the National Academy of Sciences of the United States of America*. 107:20726-20731.

Bennett, M.K., J.E. Garcia-Arraras, L.A. Elferink, K. Peterson, A.M. Fleming, C.D. Hazuka, and R.H. Scheller. 1993. The syntaxin family of vesicular transport receptors. *Cell*. 74:863-873.

Botelho, R.J., and S. Grinstein. 2011. Phagocytosis. *Current biology : CB*. 21:R533-538.

Braun, V., V. Fraisier, G. Raposo, I. Hurbain, J.B. Sibarita, P. Chavrier, T. Galli, and F. Niedergang. 2004. TI-VAMP/VAMP7 is required for optimal phagocytosis of opsonised particles in macrophages. *The EMBO journal*. 23:4166-4176.

Butler, C.A., A.S. Popescu, E.J.A. Kitchener, D.H. Allendorf, M. Puigdellivol, and G.C. Brown. 2021. Microglial phagocytosis of neurons in neurodegeneration, and its regulation. *Journal of neurochemistry*. 158:621-639.

Cebrian, I., G. Visentin, N. Blanchard, M. Jouve, A. Bobard, C. Moita, J. Enninga, L.F. Moita, S. Amigorena, and A. Savina. 2011. Sec22b regulates phagosomal maturation and antigen crosspresentation by dendritic cells. *Cell*. 147:1355-1368.

Czibener, C., N.M. Sherer, S.M. Becker, M. Pypaert, E. Hui, E.R. Chapman, W. Mothes, and N.W. Andrews. 2006. Ca2+ and synaptotagmin VII-dependent delivery of lysosomal membrane to nascent phagosomes. *The Journal of cell biology*. 174:997-1007.

Descoteaux, A.F.V.a.A. 2009. Macrophages and Dendritic Cells: Methods and Protocols. *In* Methods in molecular biology. Vol. 531. N.E. Reiner, editor. 329-346.

Desjardins, M. 2003. ER-mediated phagocytosis: a new membrane for new functions. *Nature reviews. Immunology*. 3:280-291.

Desjardins, M., L.A. Huber, R.G. Parton, and G. Griffiths. 1994. Biogenesis of phagolysosomes proceeds through a sequential series of interactions with the endocytic apparatus. *The Journal of cell biology*. 124:677-688.

Diao, J., R. Liu, Y. Rong, M. Zhao, J. Zhang, Y. Lai, Q. Zhou, L.M. Wilz, J. Li, S. Vivona, R.A. Pfuetzner, A.T. Brunger, and Q. Zhong. 2015. ATG14 promotes membrane tethering and fusion of autophagosomes to endolysosomes. *Nature*. 520:563-566.

Dolai, S., T. Liang, A.I. Orabi, D. Holmyard, L. Xie, D. Greitzer-Antes, Y. Kang, H. Xie, T.A. Javed, P.P. Lam, D.C. Rubin, P. Thorn, and H.Y. Gaisano. 2018. Pancreatitis-Induced Depletion of Syntaxin 2 Promotes Autophagy and Increases Basolateral Exocytosis. *Gastroenterology*. 154:1805-1821 e1805.

Fairn, G.D., and S. Grinstein. 2012. How nascent phagosomes mature to become phagolysosomes. *Trends in immunology*. 33:397-405.

Flannagan, R.S., V. Jaumouille, and S. Grinstein. 2012. The cell biology of phagocytosis. *Annual review of pathology*. 7:61-98.

Flaumenhaft, R., N. Rozenvayn, D. Feng, and A.M. Dvorak. 2007. SNAP-23 and syntaxin-2 localize to the extracellular surface of the platelet plasma membrane. *Blood*. 110:1492-1501.

Freeman, S.A., and S. Grinstein. 2014. Phagocytosis: receptors, signal integration, and the cytoskeleton. *Immunological reviews*. 262:193-215.

Fritsch, C., E.A. Swietlicki, O. Lefebvre, M. Kedinger, H. Iordanov, M.S. Levin, and D.C. Rubin. 2002. Epimorphin expression in intestinal myofibroblasts induces epithelial morphogenesis. *The Journal of clinical investigation*. 110:1629-1641.

Gray, M.A., C.H. Choy, R.M. Dayam, E. Ospina-Escobar, A. Somerville, X. Xiao, S.M. Ferguson, and R.J. Botelho. 2016. Phagocytosis Enhances Lysosomal and Bactericidal Properties by Activating the Transcription Factor TFEB. *Current biology : CB*. 26:1955-1964.

Hackam, D.J., O.D. Rotstein, M.K. Bennett, A. Klip, S. Grinstein, and M.F. Manolson. 1996. Characterization and subcellular localization of target membrane soluble NSF attachment protein receptors (t-SNAREs) in macrophages. Syntaxins 2, 3, and 4 are present on phagosomal membranes. *Journal of immunology*. 156:4377-4383.

Hackam, D.J., O.D. Rotstein, C. Sjolin, A.D. Schreiber, W.S. Trimble, and S. Grinstein. 1998. v-SNARE-dependent secretion is required for phagocytosis. *Proceedings of the National Academy of Sciences of the United States of America*. 95:11691-11696.

Hatsuzawa, K., H. Hashimoto, H. Hashimoto, S. Arai, T. Tamura, A. Higa-Nishiyama, and I. Wada. 2009. Sec22b is a negative regulator of phagocytosis in macrophages. *Molecular biology of the cell*. 20:4435-4443.

Hirai, Y., D. Radisky, R. Boudreau, M. Simian, M.E. Stevens, Y. Oka, K. Takebe, S. Niwa, and M.J. Bissell. 2001. Epimorphin mediates mammary luminal morphogenesis through control of C/EBPbeta. *The Journal of cell biology*. 153:785-794.

Hirai, Y., K. Takebe, M. Takashina, S. Kobayashi, and M. Takeichi. 1992. Epimorphin: a mesenchymal protein essential for epithelial morphogenesis. *Cell*. 69:471-481.

Huang, J., V. Canadien, G.Y. Lam, B.E. Steinberg, M.C. Dinauer, M.A. Magalhaes, M. Glogauer, S. Grinstein, and J.H. Brumell. 2009. Activation of antibacterial autophagy by NADPH oxidases. *Proceedings of the National Academy of Sciences of the United States of America*. 106:6226-6231.

Jahn, R., and R.H. Scheller. 2006. SNAREs--engines for membrane fusion. *Nature reviews. Molecular cell biology*. 7:631-643.

Kang, F., L. Xie, T. Qin, Y. Miao, Y. Kang, T. Takahashi, T. Liang, H. Xie, and H.Y. Gaisano. 2022. Plasma membrane flipping of Syntaxin-2 regulates its inhibitory action on insulin granule exocytosis. *Nature communications*. 13:6512.

Kleinberger, G., Y. Yamanishi, M. Suarez-Calvet, E. Czirr, E. Lohmann, E. Cuyvers, H. Struyfs, N. Pettkus, A. Wenninger-Weinzierl, F. Mazaheri, S. Tahirovic, A. Lleo, D. Alcolea, J. Fortea, M. Willem, S. Lammich, J.L. Molinuevo, R. Sanchez-Valle, A. Antonell, A. Ramirez, M.T. Heneka, K. Sleegers, J. van der Zee, J.J. Martin, S. Engelborghs, A. Demirtas-Tatlidede, H. Zetterberg, C. Van Broeckhoven, H. Gurvit, T. Wyss-Coray, J. Hardy, M. Colonna, and C. Haass. 2014. TREM2 mutations implicated in neurodegeneration impair cell surface transport and phagocytosis. *Science translational medicine*. 6:243ra286.

Laurent-Matha, V., D. Derocq, C. Prebois, N. Katunuma, and E. Liaudet-Coopman. 2006. Processing of human cathepsin D is independent of its catalytic function and auto-activation: involvement of cathepsins L and B. *Journal of biochemistry*. 139:363-371.

Low, S.H., X. Li, M. Miura, N. Kudo, B. Quinones, and T. Weimbs. 2003. Syntaxin 2 and endobrevin are required for the terminal step of cytokinesis in mammalian cells. *Developmental cell*. 4:753-759.

Mantegazza, A.R., J.G. Magalhaes, S. Amigorena, and M.S. Marks. 2013. Presentation of phagocytosed antigens by MHC class I and II. *Traffic*. 14:135-152.

Munoz, L.E., K. Lauber, M. Schiller, A.A. Manfredi, and M. Herrmann. 2010. The role of defective clearance of apoptotic cells in systemic autoimmunity. *Nature reviews. Rheumatology*. 6:280-289.

Murray, R.Z., J.G. Kay, D.G. Sangermani, and J.L. Stow. 2005. A role for the phagosome in cytokine secretion. *Science*. 310:1492-1495.

Niedergang, F., E. Colucci-Guyon, T. Dubois, G. Raposo, and P. Chavrier. 2003. ADP ribosylation factor 6 is activated and controls membrane delivery during phagocytosis in macrophages. *The Journal of cell biology*. 161:1143-1150.

Niedergang, F., and S. Grinstein. 2018. How to build a phagosome: new concepts for an old process. *Current opinion in cell biology*. 50:57-63.

Pagan, J.K., F.G. Wylie, S. Joseph, C. Widberg, N.J. Bryant, D.E. James, and J.L. Stow. 2003. The t-SNARE syntaxin 4 is regulated during macrophage activation to function in membrane traffic and cytokine secretion. *Current biology : CB*. 13:156-160.

Paumet, F., J. Wesolowski, A. Garcia-Diaz, C. Delevoye, N. Aulner, H.A. Shuman, A. Subtil, and J.E. Rothman. 2009. Intracellular bacteria encode inhibitory SNARE-like proteins. *PloS one*. 4:e7375.

Puertollano, R., S.M. Ferguson, J. Brugarolas, and A. Ballabio. 2018. The complex relationship between TFEB transcription factor phosphorylation and subcellular localization. *The EMBO journal*. 37.

Rao, S.K., C. Huynh, V. Proux-Gillardeaux, T. Galli, and N.W. Andrews. 2004. Identification of SNAREs involved in synaptotagmin VII-regulated lysosomal exocytosis. *The Journal of biological chemistry*. 279:20471-20479.

Rogers, L.D., and L.J. Foster. 2007. The dynamic phagosomal proteome and the contribution of the endoplasmic reticulum. *Proceedings of the National Academy of Sciences of the United States of America*. 104:18520-18525.

Roy, D., D.R. Liston, V.J. Idone, A. Di, D.J. Nelson, C. Pujol, J.B. Bliska, S. Chakrabarti, and N.W. Andrews. 2004. A process for controlling intracellular bacterial infections induced by membrane injury. *Science*. 304:1515-1518.

Sardiello, M., M. Palmieri, A. di Ronza, D.L. Medina, M. Valenza, V.A. Gennarino, C. Di Malta, F. Donaudy, V. Embrione, R.S. Polishchuk, S. Banfi, G. Parenti, E. Cattaneo, and A. Ballabio. 2009. A gene network regulating lysosomal biogenesis and function. *Science*. 325:473-477.

Settembre, C., C. Di Malta, V.A. Polito, M. Garcia Arencibia, F. Vetrini, S. Erdin, S.U. Erdin, T. Huynh, D. Medina, P. Colella, M. Sardiello, D.C. Rubinsztein, and A. Ballabio. 2011. TFEB links autophagy to lysosomal biogenesis. *Science*. 332:1429-1433.

Settembre, C., R. Zoncu, D.L. Medina, F. Vetrini, S. Erdin, S. Erdin, T. Huynh, M. Ferron, G. Karsenty, M.C. Vellard, V. Facchinetti, D.M. Sabatini, and A. Ballabio. 2012. A lysosome-to-nucleus signalling mechanism senses and regulates the lysosome via mTOR and TFEB. *The EMBO journal*. 31:1095-1108.

Shui, W., L. Sheu, J. Liu, B. Smart, C.J. Petzold, T.Y. Hsieh, A. Pitcher, J.D. Keasling, and C.R. Bertozzi. 2008. Membrane proteomics of phagosomes suggests a connection to autophagy. *Proceedings of the National Academy of Sciences of the United States of America*. 105:16952-16957.

Steegmaier, M., J. Klumperman, D.L. Foletti, J.S. Yoo, and R.H. Scheller. 1999. Vesicle-associated membrane protein 4 is implicated in trans-Golgi network vesicle trafficking. *Molecular biology of the cell*. 10:1957-1972.

Stuart, L.M., and R.A. Ezekowitz. 2005. Phagocytosis: elegant complexity. *Immunity*. 22:539-550.

Sudhof, T.C., and J.E. Rothman. 2009. Membrane fusion: grappling with SNARE and SM proteins. *Science*. 323:474-477.

Sun, W., Q. Yan, T.A. Vida, and A.J. Bean. 2003. Hrs regulates early endosome fusion by inhibiting formation of an endosomal SNARE complex. *The Journal of cell biology*. 162:125-137.

Swanson, J.A. 2008. Shaping cups into phagosomes and macropinosomes. *Nature reviews. Molecular cell biology*. 9:639-649.

Swanson, J.A., and A.D. Hoppe. 2004. The coordination of signaling during Fc receptor-mediated phagocytosis. *Journal of leukocyte biology*. 76:1093-1103.

Tran, T.H., Q. Zeng, and W. Hong. 2007. VAMP4 cycles from the cell surface to the trans-Golgi network via sorting and recycling endosomes. *Journal of cell science*. 120:1028-1041.

Varlamov, O., A. Volchuk, V. Rahimian, C.A. Doege, F. Paumet, W.S. Eng, N. Arango, F. Parlati, M. Ravazzola, L. Orci, T.H. Sollner, and J.E. Rothman. 2004. i-SNAREs: inhibitory SNAREs that fine-tune the specificity of membrane fusion. *The Journal of cell biology*. 164:79-88.

Vieira, O.V., R.J. Botelho, and S. Grinstein. 2002. Phagosome maturation: aging gracefully. *The Biochemical journal*. 366:689-704.

Wojnacki, J., A.L. Lujan, N. Brouwers, C. Aranda-Vallejo, G. Bigliani, M.P. Rodriguez, O. Foresti, and V. Malhotra. 2023. Tetraspanin-8 sequesters syntaxin-2 to control biphasic release propensity of mucin granules. *Nature communications*. 14:3710.

Wong, C.O., S. Gregory, H. Hu, Y. Chao, V.E. Sepulveda, Y. He, D. Li-Kroeger, W.E. Goldman, H.J. Bellen, and K. Venkatachalam. 2017. Lysosomal Degradation Is Required for Sustained Phagocytosis of Bacteria by Macrophages. *Cell host & microbe*. 21:719-730 e716.

Yang, C., and X. Wang. 2021. Lysosome biogenesis: Regulation and functions. *The Journal of cell biology*. 220.

Ye, S., Z.A. Karim, R. Al Hawas, J.E. Pessin, A.H. Filipovich, and S.W. Whiteheart. 2012. Syntaxin-11, but not syntaxin-2 or syntaxin-4, is required for platelet secretion. *Blood*. 120:2484-2492.

Zhang, W., X. Yang, Y. Li, L. Yu, B. Zhang, J. Zhang, W.J. Cho, V. Venkatarangan, L. Chen, B.B. Burugula, S. Bui, Y. Wang, C. Duan, J.O. Kitzman, and M. Li. 2022. GCAF(TMEM251) regulates lysosome biogenesis by activating the mannose-6-phosphate pathway. *Nature communications*. 13:5351.

Zhu, D., L. Xie, Y. Kang, S. Dolai, J. Bondo Hansen, T. Qin, H. Xie, T. Liang, D.C. Rubin, L. Osborne, and H.Y. Gaisano. 2017. Syntaxin 2 Acts as Inhibitory SNARE for Insulin Granule Exocytosis. *Diabetes*. 66:948-959.

Figure 1

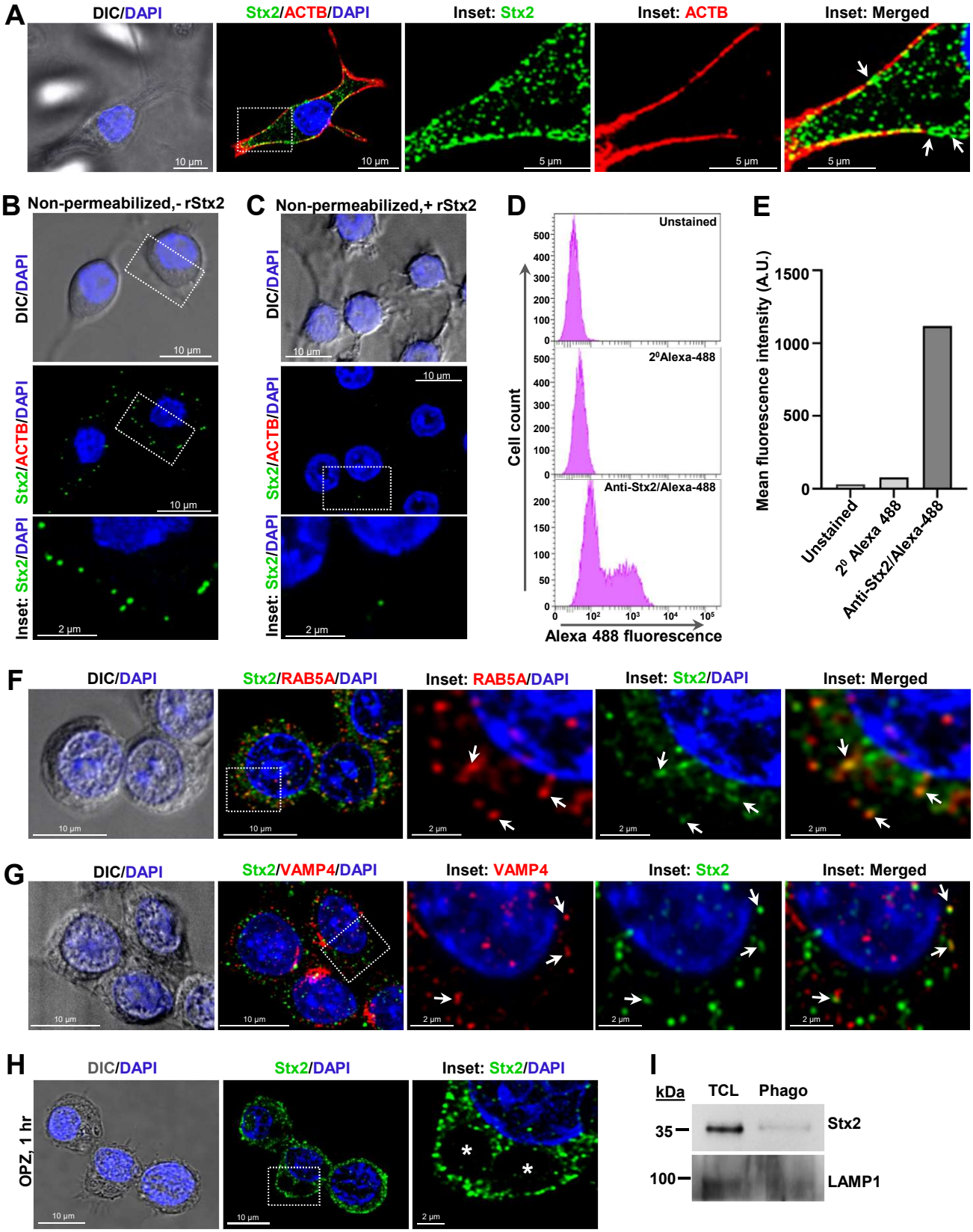
A
DIC/DAPI
Stx2/ACTB/DAPI
Inset: Stx2
Inset: ACTB
Inset: Merged
10 µm
5 µm
B
Non-permeabilized,- rStx2
C
Non-permeabilized,+ rStx2
DIC/DAPI
Stx2/ACTB/DAPI
Inset: Stx2/DAPI
2 µm
D
Unstained
2⁰Alexa-488
Anti-Stx2/Alexa-488
Cell count
Alexa 488 fluorescence
E
Mean fluorescence intensity (A.U.)
Unstained
2⁰ Alexa 488
Anti-Stx2/Alexa-488
F
Stx2/RAB5A/DAPI
Inset: RAB5A/DAPI
Inset: Stx2/DAPI
G
Stx2/VAMP4/DAPI
Inset: VAMP4
H
OPZ, 1 hr
I
kDa
TCL
Phago
35
100
Stx2
LAMP1

Figure 2

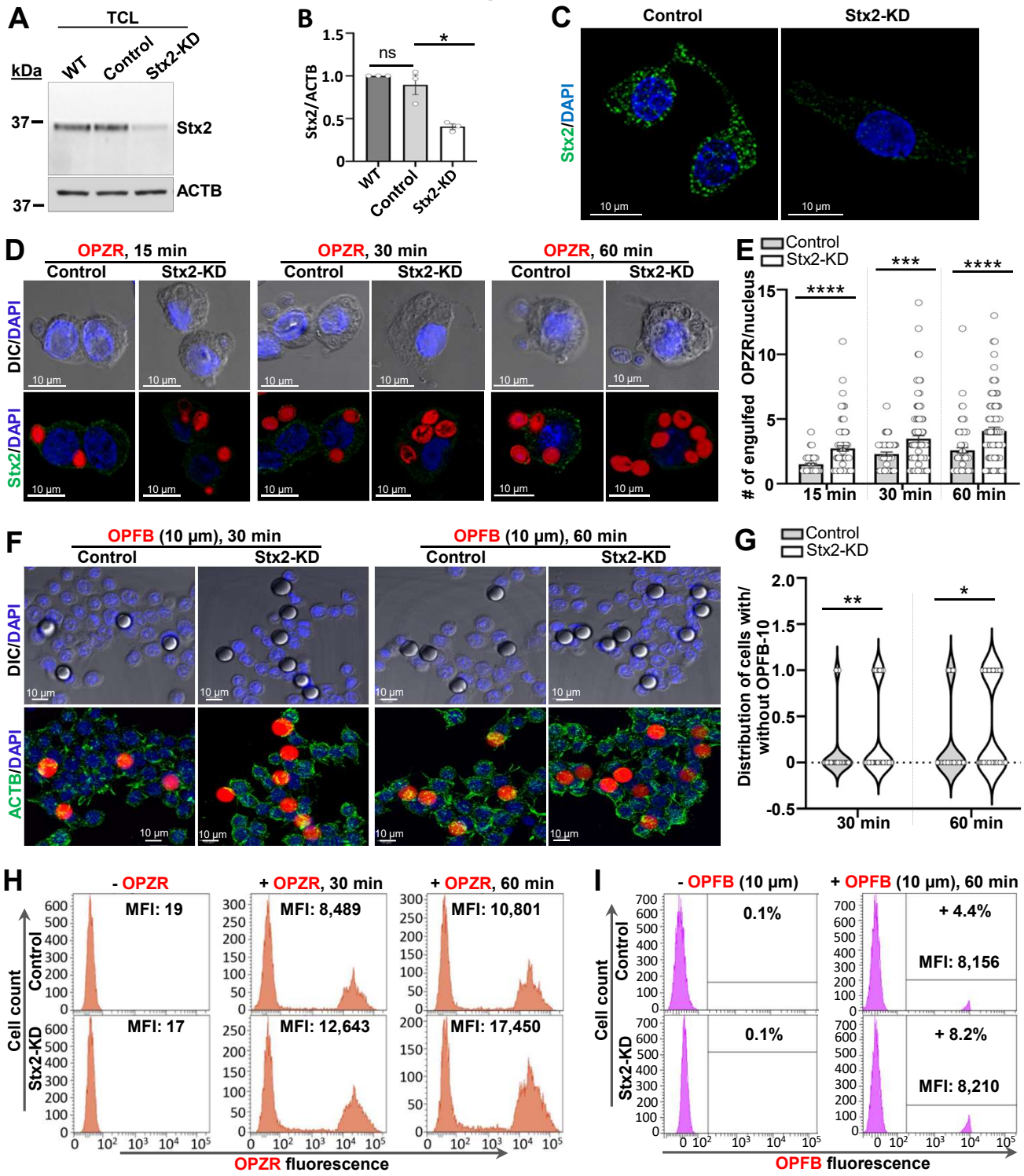
A
TCL
kDa
WT
Control
Stx2-KD
37
Stx2
37
ACTB
B
Stx2/ACTB
1.5
1.0
0.5
0
ns
*
WT
Control
Stx2-KD
C
Control
Stx2-KD
Stx2/DAPI
10 µm
D
OPZR, 15 min
OPZR, 30 min
OPZR, 60 min
Control
Stx2-KD
DIC/DAPI
Stx2/DAPI
10 µm
E
Control
Stx2-KD
# of engulfed OPZR/nucleus
****
***
****
15 min
30 min
60 min
F
OPFB (10 µm), 30 min
OPFB (10 µm), 60 min
Control
Stx2-KD
DIC/DAPI
ACTB/DAPI
10 µm
G
Control
Stx2-KD
Distribution of cells with/ without OPFB-10
**
*
30 min
60 min
H
- OPZR
+ OPZR, 30 min
+ OPZR, 60 min
Cell count
Control
Stx2-KD
MFI: 19
MFI: 8,489
MFI: 10,801
MFI: 17
MFI: 12,643
MFI: 17,450
OPZR fluorescence
I
- OPFB (10 µm)
+ OPFB (10 µm), 60 min
Cell count
Control
Stx2-KD
0.1%
+ 4.4%
MFI: 8,156
0.1%
+ 8.2%
MFI: 8,210
OPFB fluorescence

Figure 3

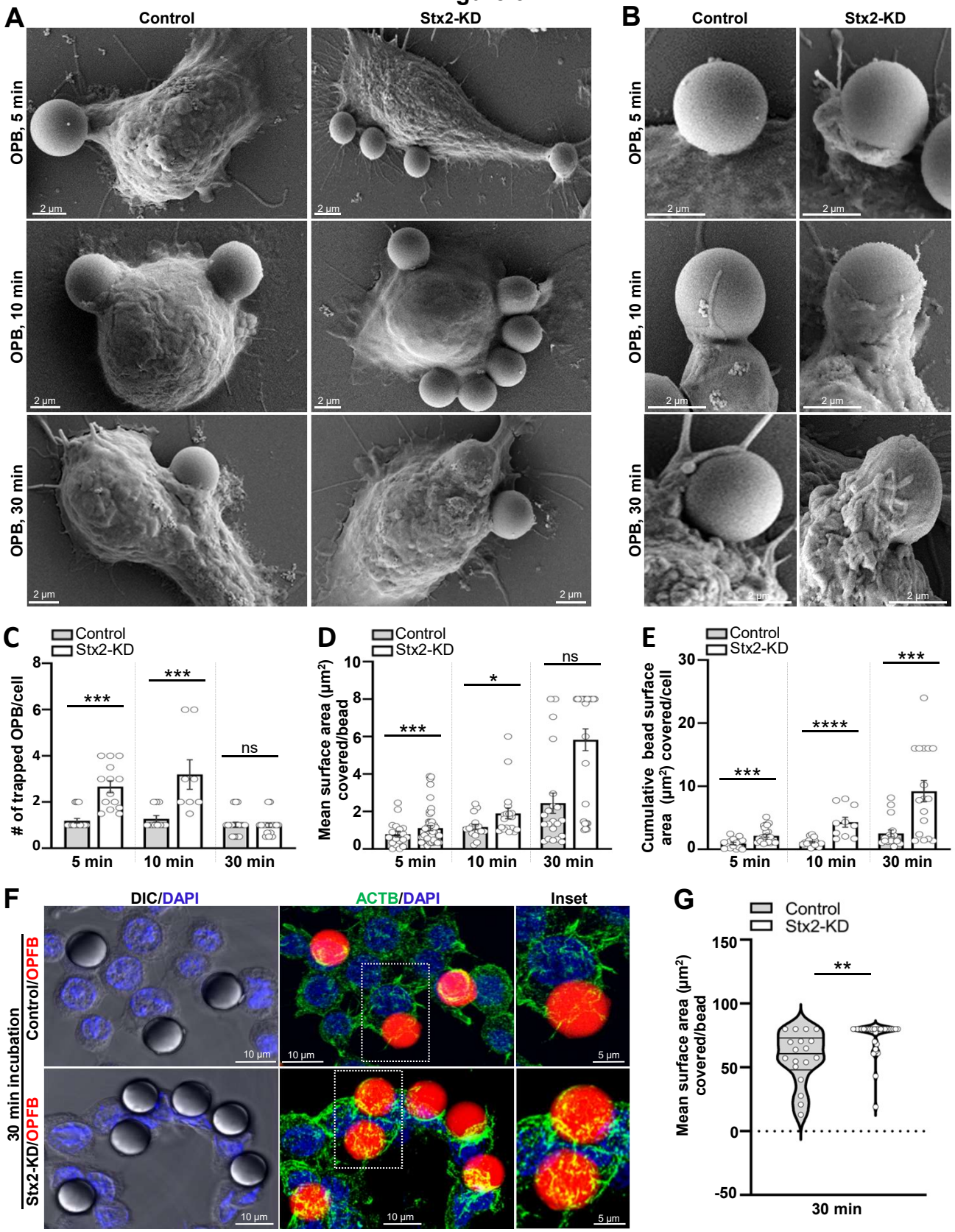
A
Control
Stx2-KD
OPB, 5 min
OPB, 10 min
OPB, 30 min
2 µm
B
Control
Stx2-KD
OPB, 5 min
OPB, 10 min
OPB, 30 min
2 µm
C
Control
Stx2-KD
# of trapped OPB/cell
***
***
ns
5 min
10 min
30 min
D
Control
Stx2-KD
Mean surface area (µm²) covered/bead
***
*
ns
5 min
10 min
30 min
E
Control
Stx2-KD
Cumulative bead surface area (µm²) covered/cell
***
****
***
5 min
10 min
30 min
F
DIC/DAPI
ACTB/DAPI
Inset
30 min incubation
Control/OPFB
Stx2-KD/OPFB
10 µm
5 µm
G
Control
Stx2-KD
Mean surface area (µm²) covered/bead
**
30 min

Figure 4

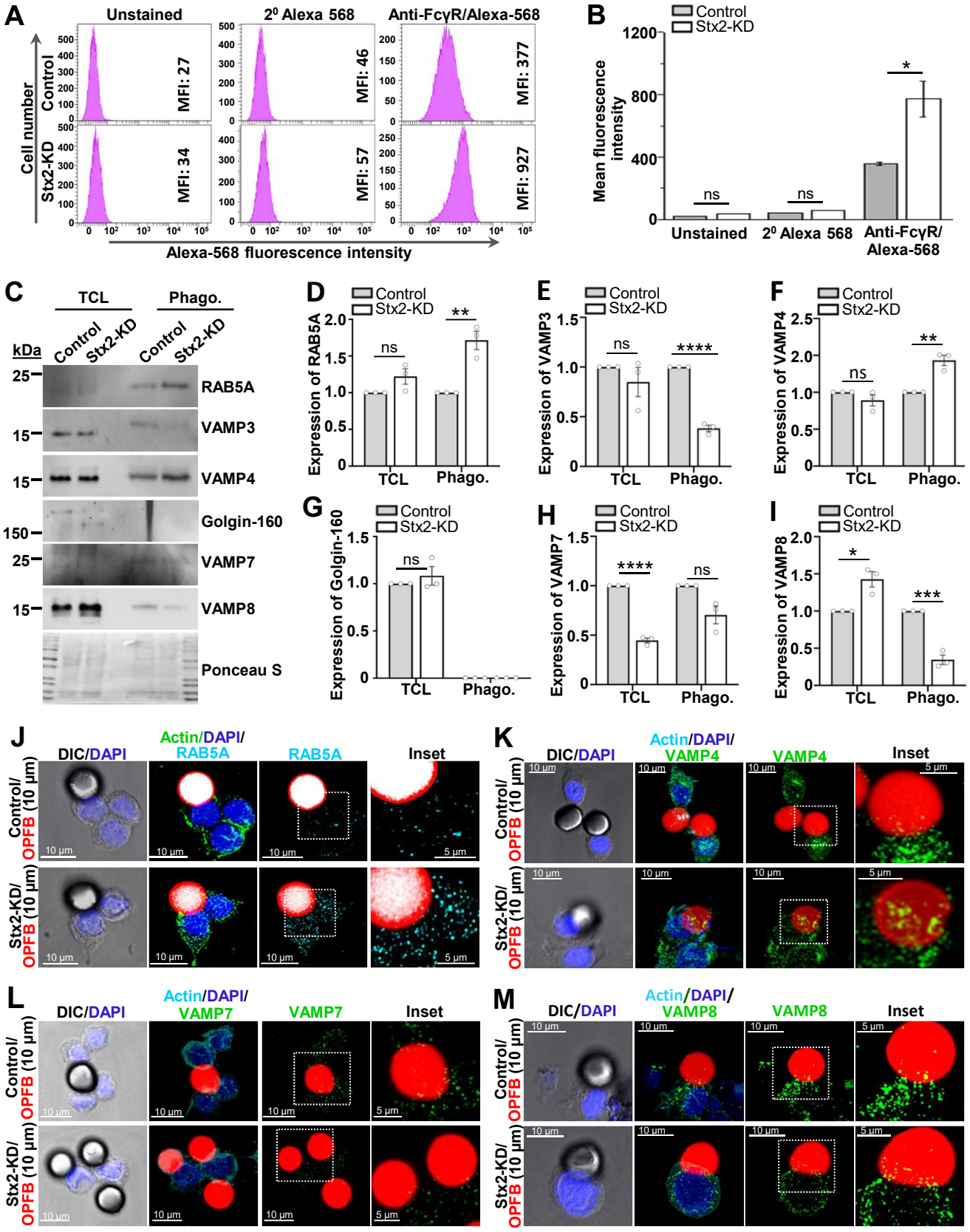
A
Unstained
2⁰ Alexa 568
Anti-FcγR/Alexa-568
Cell number
Control
Stx2-KD
MFI: 27
MFI: 46
MFI: 377
MFI: 34
MFI: 57
MFI: 927
Alexa-568 fluorescence intensity
B
Control
Stx2-KD
Mean fluorescence intensity
ns
ns
*
Unstained
2⁰ Alexa 568
Anti-FcγR/ Alexa-568
C
TCL
Phago.
kDa
Control
Stx2-KD
RAB5A
VAMP3
VAMP4
Golgin-160
VAMP7
VAMP8
Ponceau S
D
Expression of RAB5A
E
Expression of VAMP3
F
Expression of VAMP4
G
Expression of Golgin-160
H
Expression of VAMP7
I
Expression of VAMP8
J
DIC/DAPI
Actin/DAPI/ RAB5A
RAB5A
Inset
Control/ OPFB (10 µm)
Stx2-KD/ OPFB (10 µm)
K
Actin/DAPI/ VAMP4
VAMP4
L
Actin/DAPI/ VAMP7
VAMP7
M
Actin/DAPI/ VAMP8
VAMP8

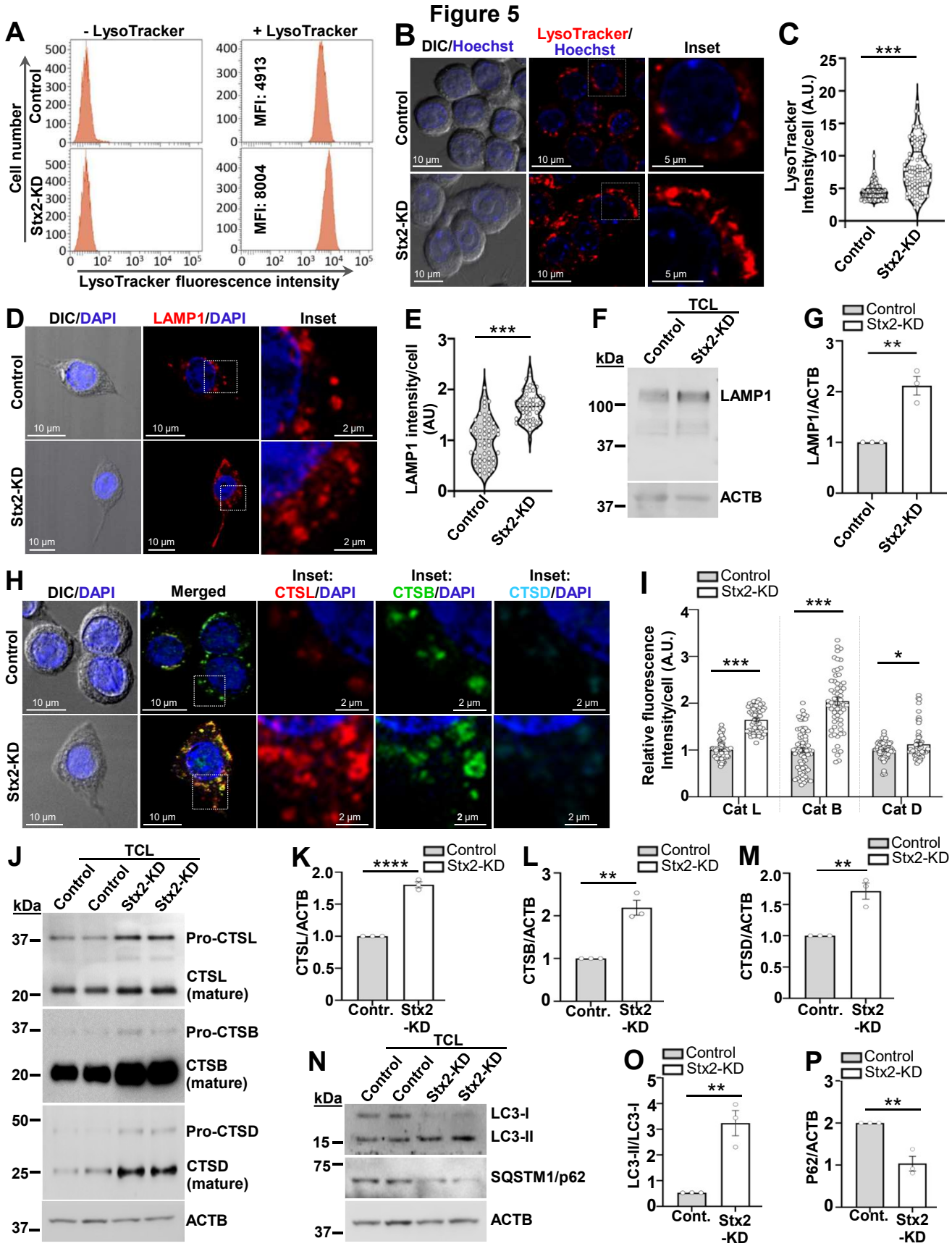
Figure 5
A
- LysoTracker
+ LysoTracker
Cell number
Control
Stx2-KD
MFI: 4913
MFI: 8004
LysoTracker fluorescence intensity
B
DIC/Hoechst
LysoTracker/Hoechst
Inset
Control
Stx2-KD
10 µm
5 µm
C
LysoTracker Intensity/cell (A.U.)
***
Control
Stx2-KD
D
DIC/DAPI
LAMP1/DAPI
Inset
Control
Stx2-KD
10 µm
2 µm
E
LAMP1 intensity/cell (AU)
***
Control
Stx2-KD
F
TCL
kDa
Control
Stx2-KD
100
37
LAMP1
ACTB
G
Control
Stx2-KD
LAMP1/ACTB
**
Control
Stx2-KD
H
DIC/DAPI
Merged
Inset: CTSL/DAPI
Inset: CTSB/DAPI
Inset: CTSD/DAPI
Control
Stx2-KD
10 µm
2 µm
I
Control
Stx2-KD
Relative fluorescence Intensity/cell (A.U.)
***
***
*
Cat L
Cat B
Cat D
J
TCL
kDa
Control
Control
Stx2-KD
Stx2-KD
37
20
Pro-CTSL
CTSL (mature)
37
20
Pro-CTSB
CTSB (mature)
50
25
Pro-CTSD
CTSD (mature)
37
ACTB
K
Control
Stx2-KD
CTSL/ACTB
****
Contr.
Stx2 -KD
L
Control
Stx2-KD
CTSB/ACTB
**
Contr.
Stx2 -KD
M
Control
Stx2-KD
CTSD/ACTB
**
Contr.
Stx2 -KD
N
TCL
kDa
Control
Control
Stx2-KD
Stx2-KD
15
75
37
LC3-I
LC3-II
SQSTM1/p62
ACTB
O
Control
Stx2-KD
LC3-II/LC3-I
**
Cont.
Stx2 -KD
P
Control
Stx2-KD
P62/ACTB
**
Cont.
Stx2 -KD

Figure 6

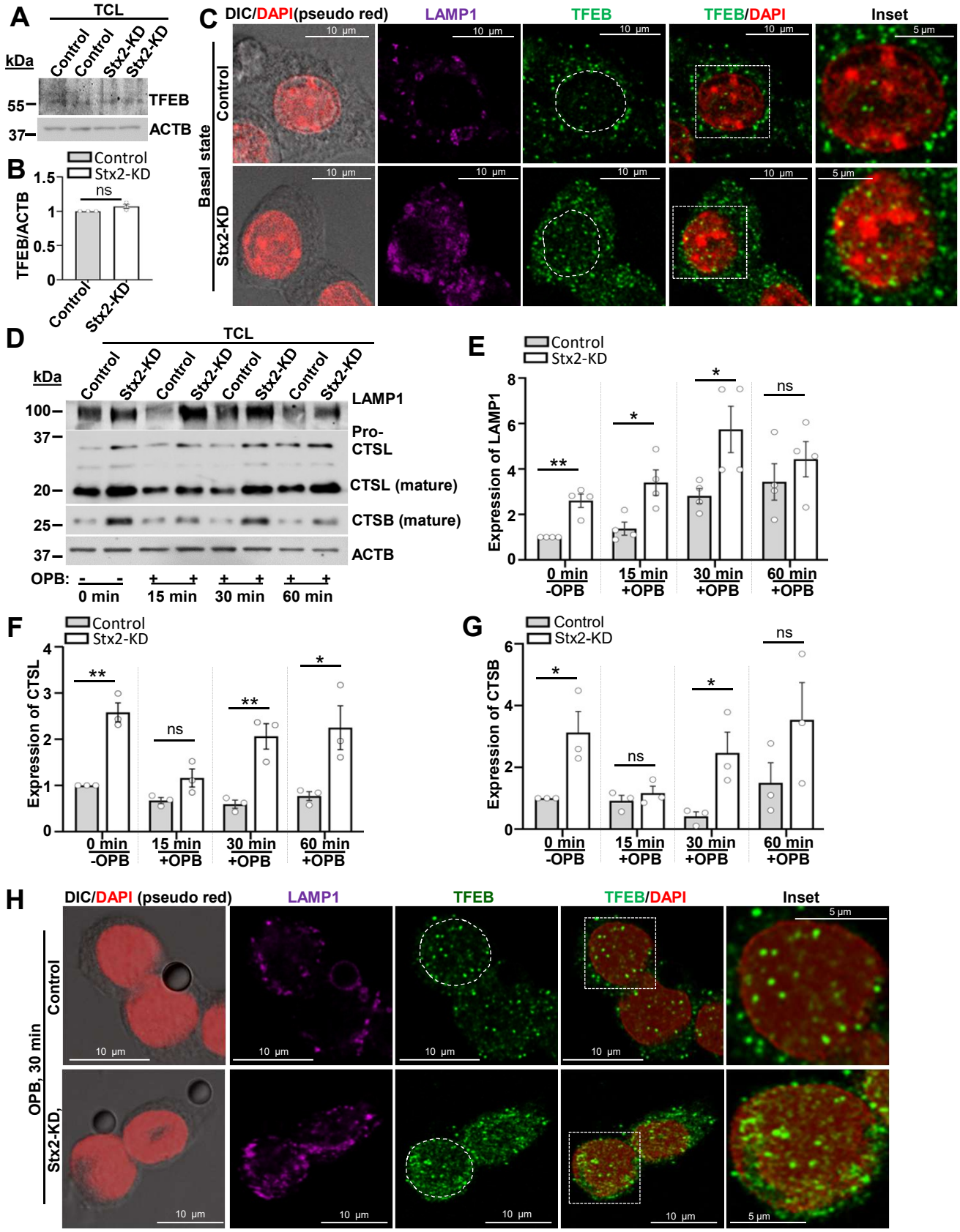
A
TCL
kDa
Control
Control
Stx2-KD
Stx2-KD
55
TFEB
37
ACTB
B
Control
Stx2-KD
ns
TFEB/ACTB
1.5
1
0.5
0
Control
Stx2-KD
C
DIC/DAPI(pseudo red)
LAMP1
TFEB
TFEB/DAPI
Inset
Basal state
Control
Stx2-KD
10 µm
5 µm
D
TCL
kDa
Control
Stx2-KD
Control
Stx2-KD
Control
Stx2-KD
Control
Stx2-KD
100
LAMP1
37
Pro-CTSL
20
CTSL (mature)
25
CTSB (mature)
37
ACTB
OPB:
0 min
15 min
30 min
60 min
E
Control
Stx2-KD
Expression of LAMP1
**
*
*
ns
0 min -OPB
15 min +OPB
30 min +OPB
60 min +OPB
F
Control
Stx2-KD
Expression of CTSL
**
ns
**
*
0 min -OPB
15 min +OPB
30 min +OPB
60 min +OPB
G
Control
Stx2-KD
Expression of CTSB
*
ns
*
ns
0 min -OPB
15 min +OPB
30 min +OPB
60 min +OPB
H
DIC/DAPI (pseudo red)
LAMP1
TFEB
TFEB/DAPI
Inset
OPB, 30 min
Control
Stx2-KD,
10 µm
5 µm

Figure 7

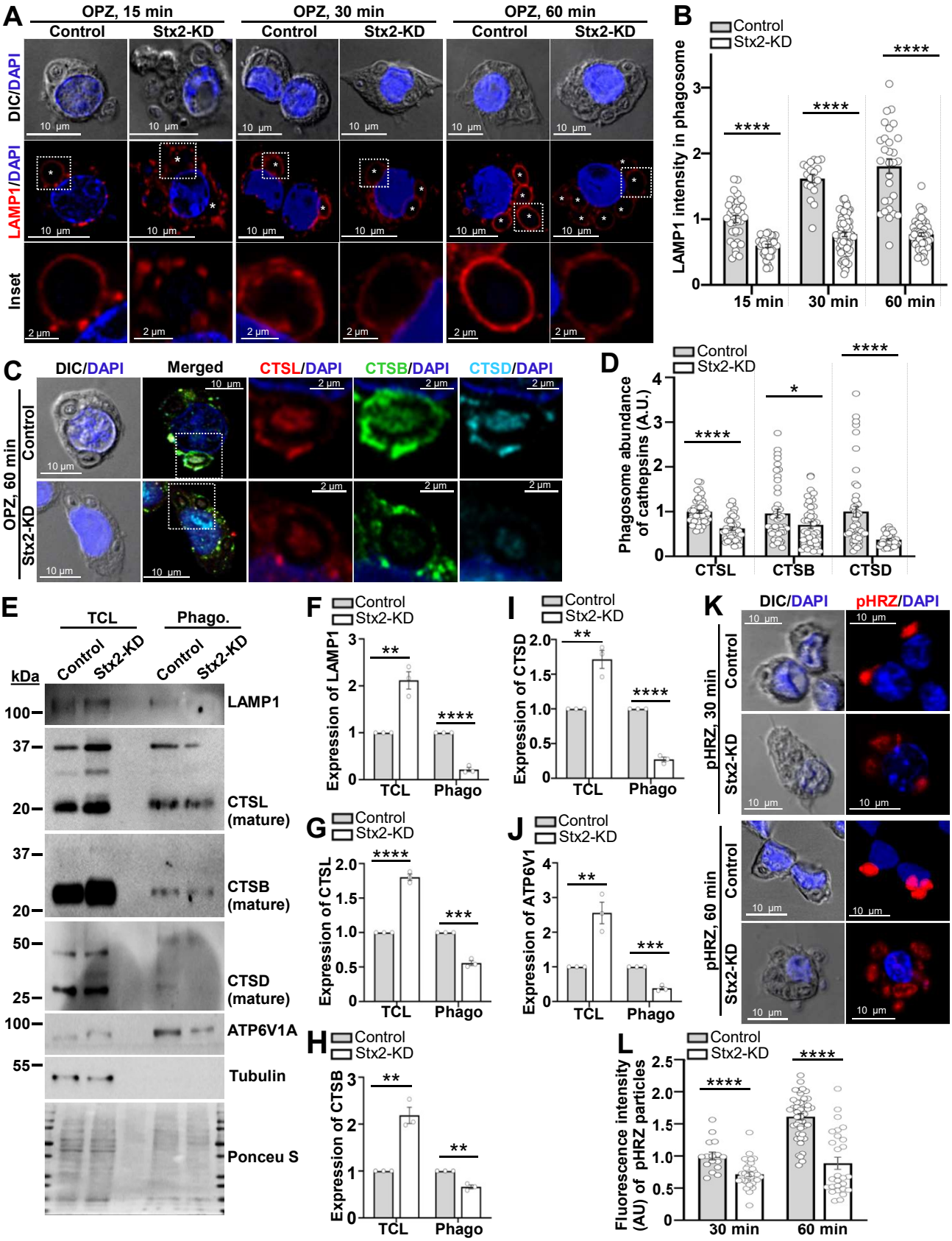
A
OPZ, 15 min
OPZ, 30 min
OPZ, 60 min
Control
Stx2-KD
DIC/DAPI
LAMP1/DAPI
Inset
10 µm
2 µm
B
Control
Stx2-KD
LAMP1 intensity in phagosome
15 min
30 min
60 min
C
DIC/DAPI
Merged
CTSL/DAPI
CTSB/DAPI
CTSD/DAPI
OPZ, 60 min
D
Phagosome abundance of cathepsins (A.U.)
CTSL
CTSB
CTSD
E
TCL
Phago.
kDa
LAMP1
CTSL (mature)
CTSB (mature)
CTSD (mature)
ATP6V1A
Tubulin
Ponceu S
F
Expression of LAMP1
G
Expression of CTSL
H
Expression of CTSB
I
Expression of CTSD
J
Expression of ATP6V1
K
pHRZ/DAPI
pHRZ, 30 min
pHRZ, 60 min
L
Fluorescence intensity (AU) of pHRZ particles

Figure 8

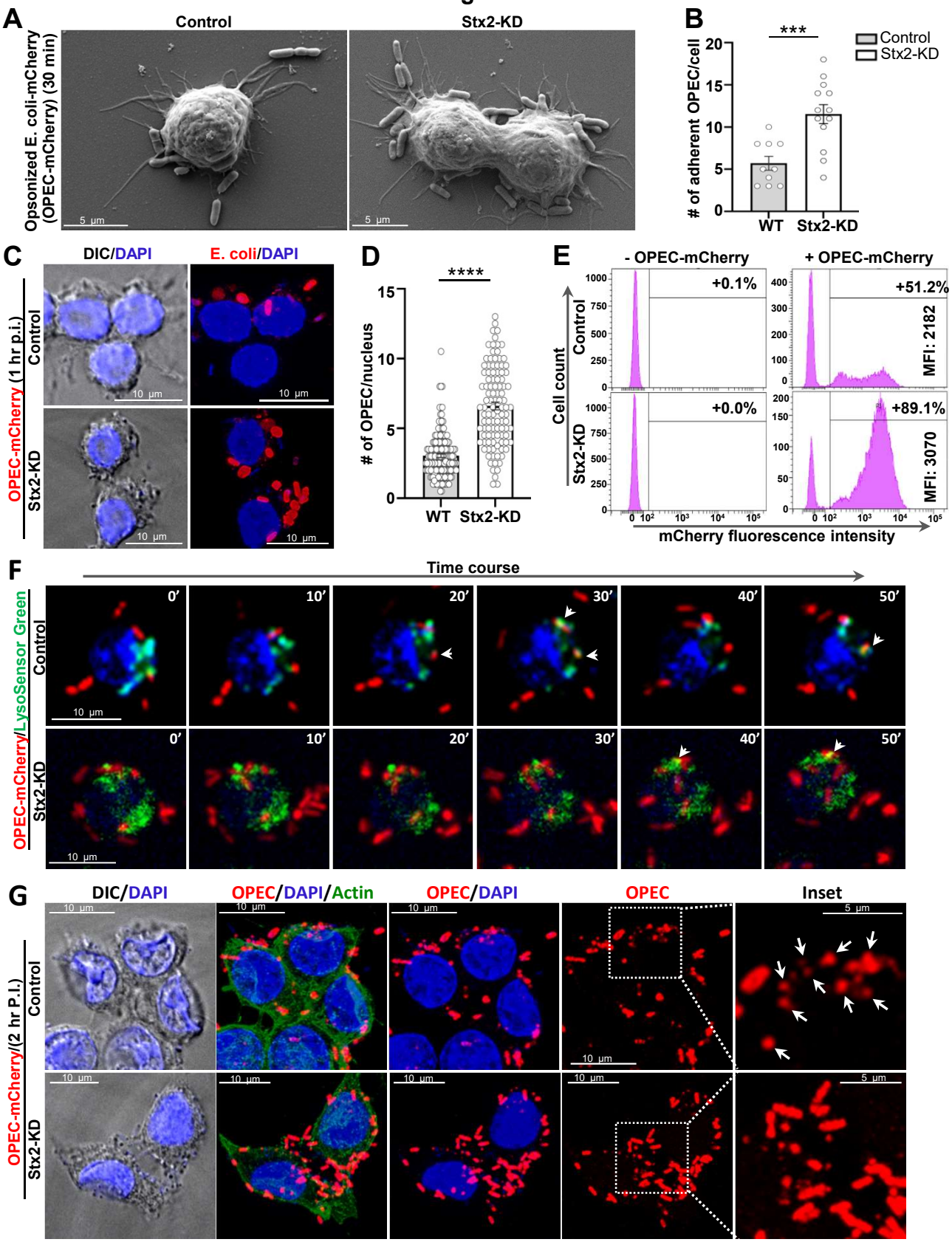
A
Control
Stx2-KD
Opsonized E. coli-mCherry (OPEC-mCherry) (30 min)
5 µm
B
***
Control
Stx2-KD
# of adherent OPEC/cell
WT
Stx2-KD
C
DIC/DAPI
E. coli/DAPI
OPEC-mCherry (1 hr p.i.)
Control
Stx2-KD
10 µm
D
****
# of OPEC/nucleus
WT
Stx2-KD
E
- OPEC-mCherry
+ OPEC-mCherry
Cell count
+0.1%
+51.2%
MFI: 2182
+0.0%
+89.1%
MFI: 3070
mCherry fluorescence intensity
F
Time course
OPEC-mCherry/LysoSensor Green
0′
10′
20′
30′
40′
50′
G
DIC/DAPI
OPEC/DAPI/Actin
OPEC/DAPI
OPEC
Inset
OPEC-mCherry/(2 hr P.I.)
5 µm